

# The properties of He II $\lambda 1640$ emitters at $z \sim 2.5 - 5$ from the VANDELS survey

A. Saxena<sup>1</sup>, L. Pentericci<sup>1</sup>, M. Mirabelli<sup>1,2</sup>, D. Schaerer<sup>3</sup>, R. Schneider<sup>1,2,4</sup>, F. Cullen<sup>5</sup>, R. Amorin<sup>6,7</sup>, M. Bolzonella<sup>8</sup>, A. Bongiorno<sup>1</sup>, A. C. Carnall<sup>5</sup>, M. Castellano<sup>1</sup>, O. Cucciati<sup>8</sup>, A. Fontana<sup>1</sup>, J. P. U. Fynbo<sup>9</sup>, B. Garilli<sup>10</sup>, A. Gargiulo<sup>10</sup>, L. Guaita<sup>11</sup>, N. P. Hathi<sup>12</sup>, T. A. Hutchison<sup>13,14</sup>, A. M. Koekemoer<sup>12</sup>, F. Marchi<sup>1</sup>, D. J. McLeod<sup>5</sup>, R. J. McLure<sup>5</sup>, C. Papovich<sup>13,14</sup>, L. Pozzetti<sup>8</sup>, M. Talia<sup>8</sup>, and G. Zamorani<sup>8</sup>

<sup>1</sup> INAF – Osservatorio Astronomico di Roma, via Frascati 33, I-00078 Monteporzio Catone, Italy

<sup>2</sup> Dipartimento di Fisica, Sapienza Università di Roma, Piazzale Aldo Moro 5, 00185 Roma, Italy

<sup>3</sup> Geneva Observatory, University of Geneva, ch. des Maillettes 51, 1290 Versoix, Switzerland

<sup>4</sup> INFN, Sezione di Roma I, Piazzale Aldo Moro 2, 00185 Roma, Italy

<sup>5</sup> SUPA (Scottish Universities Physics Alliance), Institute for Astronomy, University of Edinburgh, Royal Observatory, EH9 3HJ Edinburgh, UK

<sup>6</sup> Instituto de Investigación Multidisciplinar en Ciencia y Tecnología, Universidad de La Serena, Raúl Bitrán 1305, La Serena, Chile

<sup>7</sup> Departamento de Física y Astronomía, Universidad de La Serena, Av. Juan Cisternas 1200 Norte, La Serena, Chile

<sup>8</sup> INAF – OAS Bologna, Via P. Gobetti 93/3, I-40129, Bologna, Italy

<sup>9</sup> Cosmic DAWN Center, Niels Bohr Institute, University of Copenhagen, Juliane Maries Vej 30, 2100 Copenhagen Ø, Denmark

<sup>10</sup> INAF – IASF Milano, via Bassini 15, I-20133 Milano, Italy

<sup>11</sup> Núcleo de Astronomía, Facultad de Ingeniería, Universidad Diego Portales, Av. Ejército 441, Santiago, Chile

<sup>12</sup> Space Telescope Science Institute, 3700 San Martin Drive, Baltimore, MD 21218, USA

<sup>13</sup> Department of Physics and Astronomy, Texas A&M University, College Station, TX, 77843-4242 USA

<sup>14</sup> George P. and Cynthia Woods Mitchell Institute for Fundamental Physics and Astronomy, Texas A&M University, College Station, TX, 77843-4242 USA

e-mail: aayush.saxena@inaf.it

Received 22 November 2019 / Accepted 05 March 2020

## ABSTRACT

**Aims.** Strong He II emission is produced by low-metallicity stellar populations. Here, we aim to identify and study a sample of He II  $\lambda 1640$ -emitting galaxies at redshifts of  $z \sim 2.5 - 5$  in the deep VANDELS spectroscopic survey.

**Methods.** We identified a total of 33 *Bright* He II emitters ( $S/N > 2.5$ ) and 17 *Faint* emitters ( $S/N < 2.5$ ) in the VANDELS survey and used the available deep multi-wavelength data to study their physical properties. After identifying seven potential AGNs in our sample and discarding them from further analysis, we divided the sample of *Bright* emitters into 20 *Narrow* ( $\text{FWHM} < 1000 \text{ km s}^{-1}$ ) and 6 *Broad* ( $\text{FWHM} > 1000 \text{ km s}^{-1}$ ) He II emitters. We created stacks of *Faint*, *Narrow*, and *Broad* emitters and measured other rest-frame UV lines such as O III] and C III] in both individual galaxies and stacks. We then compared the UV line ratios with the output of stellar population-synthesis models to study the ionising properties of He II emitters.

**Results.** We do not see a significant difference between the stellar masses, star-formation rates, and rest-frame UV magnitudes of galaxies with He II and no He II emission. The stellar population models reproduce the observed UV line ratios from metals in a consistent manner, however they under-predict the total number of He II ionising photons, confirming earlier studies and suggesting that additional mechanisms capable of producing He II are needed, such as X-ray binaries or stripped stars. The models favour subsolar metallicities ( $\sim 0.1Z_{\odot}$ ) and young stellar ages ( $10^6 - 10^7$  years) for the He II emitters. However, the metallicity measured for He II emitters is comparable to that of non-He II emitters at similar redshifts. We argue that galaxies with He II emission may have undergone a recent star-formation event, or may be powered by additional sources of He II ionisation.

**Key words.** galaxies: high-redshift; galaxies: evolution

## 1. Introduction

Understanding the nature of the key drivers of reionisation, a process through which the intergalactic medium (IGM) in the Universe made a phase transition from neutral to completely ionised (by  $z \sim 6$ ), is one of the most exciting challenges in cosmology today. The general consensus now is that reionisation was predominantly driven by low-mass star-forming galaxies at  $z > 6$  (Robertson et al. 2010, 2015; Bouwens et al. 2015). The key requirement from such galaxies is the production and escape of a sufficiently large number of photons with energies  $E > 13.6$

eV that are capable of ionising all the neutral hydrogen in the Universe. Galaxies with low metallicities and a high escape fraction of these ionising photons ( $\geq 10\%$ ) should in principle be able to complete the reionisation process by  $z \sim 6$  (see Stanway et al. 2016, for example). Recently, Finkelstein et al. (2019) explored scenarios in which galaxies with low ionising photon escape fractions ( $< 5\%$ ) could potentially ionise the IGM.

There is growing observational evidence that galaxies in the early Universe ( $z > 2$ ) have lower metallicities, both in the gas phase and in stars, compared to the local galaxy population that we see today (Erb et al. 2010; Henry et al. 2013; Steidel et al.

2014; Cullen et al. 2014, 2019; Amorín et al. 2017; Sanders et al. 2018). Lower metallicities naturally lead to the production of harder UV ionisation fields (Steidel et al. 2014, 2016). From a theoretical point of view, the first galaxies and proto-galaxies formed in the Universe must essentially consist of metal-free (or Pop-III) stars that are capable of producing a large number of UV ionising photons that would ultimately be responsible for the very early stages of reionisation (Tumlinson & Shull 2000; Barkana & Loeb 2001; Sokasian et al. 2004; Robertson et al. 2010; Bromm & Yoshida 2011; Wise et al. 2012).

One important consequence of the presence of metal-free gas in the early Universe is that stars formed out of it can have very high masses and temperatures (e.g. Bromm & Larson 2004; Bromm & Yoshida 2011), leading to a top-heavy initial mass function (IMF). With such an IMF, a large number of very high-energy photons can be produced. Such photons should in principle be capable of ionising UV emission lines requiring very high ionisation energies, such as He II  $\lambda 1640$  (where the He<sup>+</sup> ionisation potential is  $> 54.4$  eV,  $\lambda < 228$  Å) and give rise to strong line fluxes (Schaerer 2002).

The link between strong He II emission and low metallicities has been shown to exist both using theory and observations at a broad range of redshifts. Schaefer (2003) showed that strong He II accompanied by strong Ly $\alpha$  are expected in the spectra of galaxies that are transitioning from Pop-III dominated to more ‘normal’ galaxies that have already been observed. In the local Universe, it has been shown that extremely metal-poor dwarf galaxies often have strong He II  $\lambda 4686$  emission in their spectra (Guseva et al. 2000; Izotov & Thuan 2004; Shirazi & Brinchmann 2012; Kehrig et al. 2015, 2018; Senchyna et al. 2017, 2019a; Berg et al. 2019). In individually detected lensed galaxies with low metallicities at high redshifts, detection of He II  $\lambda 1640$  has also been reported (Patrício et al. 2016; Berg et al. 2018).

Deep spectroscopic surveys of galaxies at  $z > 2$  have also led to a number of detections of the He II  $\lambda 1640$  line. Cassata et al. (2013) argued the case of a possible contribution from Pop III-like stars in order to explain the narrow He II emission lines observed in their sample of star-forming galaxies at  $z \sim 2 - 4.6$ . For their broad He II emitters, the most likely explanation for powering the emission was either winds driven from Wolf-Rayet (WR) stars (see Schaefer 1996; Shirazi & Brinchmann 2012, for example) or a contribution from the accretion disc of active galactic nuclei (AGNs), as is seen in broad He II -emitting galaxies at low redshifts. Nanayakkara et al. (2019) showed that to explain the observed line ratios and line fluxes for He II emitters seen in star-forming galaxies at  $z \sim 2 - 4$ , UV emission line diagnostic tests point towards ionisation by stellar populations with subsolar metallicities.

In addition to low-metallicity stars, several other physical mechanisms have been proposed in the literature that could lead to strong He II emission in the spectra of galaxies. For example, inclusion of stellar rotation, which captures the effects of rotational mixing leading to higher effective temperatures and moderate mass-loss rates may be able to explain the observed He II emission in low-metallicity galaxies (Szécsi et al. 2015). The models including interacting binary stars, such as Binary Population and Spectral Synthesis<sup>1</sup> (BPASS; Eldridge et al. 2017; Stanway & Eldridge 2018; Xiao et al. 2018), improve overall spectral fits and observed emission line ratios in star-forming galaxies at high redshifts, predominantly due to higher stellar effective temperatures producing harder ionising spectra for an extended period of time. These effects help in better re-

producing features such as the narrow nebular He II emission line in comparison to the single star models (see Steidel et al. 2016, for example). However, binary star models fall short of reproducing the observed He II equivalent widths in high-redshift galaxies, even after considering different initial mass functions in the modelling (Stanway & Eldridge 2019; Nanayakkara et al. 2019). Careful modelling of mass transfer in binaries that may lead to ‘stellar stripping’ and rejuvenation of old stars may also provide the extra He II -ionising photons needed to explain the observed emission lines (Götberg et al. 2018, 2019).

An additional contribution from X-ray binaries (XRBs) has been suggested as one of the mechanisms that may be capable of explaining the He II line fluxes observed in low-metallicity galaxies, both in the local Universe and at high redshifts. It has been shown that the X-ray luminosities of star-forming galaxies increase with decreasing metallicities, primarily because of an enhanced contribution from high-mass XRBs at lower metallicities (Fragos et al. 2013b,a; Douma et al. 2015; Brorby et al. 2016). Schaefer et al. (2019) showed that including the contribution from XRBs in addition to single or binary stellar populations can explain the He II emission line strength and its dependence on metallicity in local low-metallicity galaxies. However, Senchyna et al. (2019b) argue that high-mass XRB populations may not be sufficient to account for the observed He II line strengths in nearby metal-poor galaxies, and revised stellar wind models or inclusion of softer X-ray sources may be needed. At higher redshifts, Fornasini et al. (2019) showed that X-ray observations of stacks of star-forming galaxies are consistent with the metallicity dependence of the XRB populations at low redshifts. Given the overall decrease in metallicity of galaxies reported at high redshifts, it is expected that the contribution from XRBs plays an increasingly important role in the spectra of high-redshift galaxies, and the He II line offers a probe for this.

Developing a better understanding of the nature of galaxies capable of producing very high-energy ionising photons is vital, and in this paper we present a new sample of He II  $\lambda 1640$ -emitting galaxies identified in the VANDELS survey. In Section 2 we present details of our sample selection, briefly describing the VANDELS survey, and present our He II identification procedure. We also describe our line measurement and stacking techniques. In Section 3 we discuss key physical properties of He II -emitting galaxies, comparing them with results from other deep surveys at comparable redshifts in the literature. In Section 4 we explore the observed UV line ratios of both individual He II emitters as well as stacks of galaxy spectra, comparing them with photo-ionisation models including both single-star and binary-star models. In Section 5 we discuss the properties of He II -emitting galaxies in the context of the overall population of galaxies at similar redshifts and discuss some possible mechanisms that could give rise to He II emission. Finally, in Section 6 we summarise the key findings of this study.

Throughout this paper, we assume a flat  $\Lambda$ CDM cosmology with  $\Omega_m = 0.3$ ,  $\Omega_\Lambda = 0.7$  and  $H_0 = 67.7$  km s<sup>-1</sup> Mpc<sup>-1</sup> taken from Planck Collaboration et al. (2016). We use the AB magnitude system (Oke & Gunn 1983) throughout this paper.

## 2. Sample selection and He II emitter identification

In this study, we use data from VANDELS, a deep VIMOS survey of the CDFS and UDS fields in CANDELS (Grogin et al. 2011; Koekemoer et al. 2011), which itself is a recently completed ESO public spectroscopic survey carried out using the *Very Large Telescope (VLT)*. Details about the survey description and initial target selection can be found in McLure et al.

<sup>1</sup> <https://bpass.auckland.ac.nz>

(2018) and details about the data reduction and redshift determination can be found in Pentericci et al. (2018). The targets for VANDELS are selected from two well-studied extragalactic fields, the UKIDSS Ultra Deep Survey (UDS) centred around RA = 02:17:38, Dec = -05:11:55, and the Chandra Deep Field South (CDFS) centred around RA = 03:32:30, Dec = -27:48:28. In the following we briefly describe the details of the survey that are relevant to this work.

The VANDELS survey contains spectra of approximately 2100 galaxies in the redshift range  $1.0 < z < 7.0$ , with on-source integration times ranging from 20 to 80 hours, where over 70% of the targets have at least 40 hours of integration time. The galaxies targeted for spectroscopy include the star-forming galaxy population at  $z > 2.4$  and massive, passive galaxies in the redshift range  $1 < z < 2.5$ . The redshift ranges are primarily dictated by the sensitivity of the VIMOS grism used for VANDELS observations (McLure et al. 2018), which has a wavelength coverage in the range 4800 – 10000 Å. The resolution provided by these observations is  $R \sim 600$ . The final spectra have high signal-to-noise ratios (S/Ns), enabling detailed absorption and emission line studies, the study of ionising sources using emission line ratios, the derivation of accurate metallicities, and better constraints on physical parameters such as stellar masses and star-formation rates.

The spectra were reduced using the EASYLIFE data reduction pipeline (Garilli et al. 2012) and data products delivered by VANDELS consist of the extracted 1D spectra, the 2D re-sampled and sky-subtracted spectra, and catalogues with essential galaxy parameters, including spectroscopic redshifts. The reliability of redshifts in the VANDELS database is recorded by four individual and independent measurers from the VANDELS team. Based on how confident the individual measurers were about the accuracy of the redshift, the following flags were assigned (which are important for this work): 0 = no redshift could be assigned; 1 = 50% probability of being correct; 2 = 70-80% probability of being correct; 3 = 95-100% probability of being correct; 4 = 100% probability of being correct; and 9 = spectrum shows a single emission line. The typical accuracy of spectroscopic redshift measurements is  $\sim 150 \text{ km s}^{-1}$ . More details about the VANDELS data products as well as redshift determination and flag assignment can be found in Pentericci et al. (2018).

For this work, we initially selected galaxies from the VANDELS database in the following way. We selected spectra of only those star-forming galaxies that have a redshift reliability flag of either 3 or 4, which guarantees that the redshift measured by the VANDELS team has a more than 95% probability of being correct. This also ensures that there must be multiple emission or absorption features visible and that the spectrum has a high S/N. From these, we select sources in the redshift range  $2.2 < z < 4.8$ , which ensures that the He II  $\lambda 1640$  emission line, if present in the galaxy spectra, lies in regions of high throughput. From the UDS field, 455 sources satisfied the selection criteria and from CDFS, 494 sources satisfied the selection criteria. We refer to this total sample of 949 galaxies as the ‘parent’ sample.

### 2.1. Line identification

The spectra of galaxies in the parent sample were then inspected for the presence of any He II emission. Since we have only selected sources with highly reliable spectroscopic redshifts, we visually inspected the wavelength region where the He II line is

to be expected using the PANDORA software<sup>2</sup>, which is a suite of PYTHON modules designed for visualising and analysing spectra, amongst other useful operations. In cases where the He II line coincided with a strong skyline feature, we discarded the spectrum as the emission line measurement would not be reliable. Skyline contamination is particularly dominant at He II redshifts  $4.0 < z < 4.5$ , resulting in lower numbers of shortlisted sources in this range. For seemingly fainter He II emission, the 2D spectra were also inspected to look for signatures of emission and to distinguish between real signal and hot pixels or weak sky residuals. The initial identification process based on 1D and 2D spectra was carried out independently by two individuals, and only those sources that are identified as He II emitters by both individuals were retained for further analysis. A final visual examination of the shortlisted He II emitters was then independently carried out by a third individual from our team.

The sources identified to have He II emission were then moved on to the next stage of the analysis, where the He II line (and any other strong line present in the spectrum) was measured. The line fitting is performed using a single Gaussian at the position of the He II emission line in the observed frame using MUSE Python Data Analysis Framework or MPDAF<sup>3</sup>, which provides tools to analyse spectra, images, and data cubes. A S/N of the integrated line flux is obtained, and the redshifts of sources with He II (or C III) emission are updated, as He II (or C III) is a more accurate tracer of the systemic redshift (see also Nanayakkara et al. 2019). When both lines are present in the spectrum, we use the He II redshift. However, we generally find a reasonable agreement between the redshifts measured using He II and C III. At this stage, the sources are separated into two subsamples based on the inferred S/N of the emission line (similar to Nanayakkara et al. 2019). The subsample of *Bright* He II emitters contains galaxies with a S/N of the He II line  $> 2.5$ , and the subsample of *Faint* He II emitters contains galaxies with He II S/N  $< 2.5$ . In the *Faint* sample, the lowest measured S/N of the He II emission line is 1.5.

In the CDFS field, out of a total of 494 sources in the parent sample, 26 were shortlisted as He II emitters after the visual check. Of these, 19 are *Bright* emitters and 7 are *Faint* emitters. In the UDS field, the total number of sources in the parent sample was 455, with 24 He II emitters, out of which 14 are *Bright* and 10 are *Faint*. Across both fields, this leaves us with a total of 33 *Bright* emitters and 17 *Faint* emitters.

### 2.2. Line measurements of Bright sources

The individual spectra of sources in the *Bright* He II emitters sample were re-analysed using a more careful line-fitting approach. The observed spectrum of each source is first converted to rest frame using the redshift determined by the peak of the He II line which was measured earlier. The rest-frame continuum is then estimated by fitting a high-degree polynomial to the sigma-clipped spectrum around the He II emission line. The continuum is subtracted and a Gaussian is fit to the emission line, which yields an integrated flux and full-width at half maximum (FWHM) with associated errors on the fit. The integrated flux is only calculated over the wavelength range where the flux is above the continuum value. This helps to minimise the impact of absorption features close to the emission line on the total flux measured. The equivalent width (EW) of the emission line is also calculated using the measured continuum.

<sup>2</sup> <http://cosmos.iasf-milano.inaf.it/pandora/>

<sup>3</sup> <https://mpdaf.readthedocs.io/en/latest/index.html>



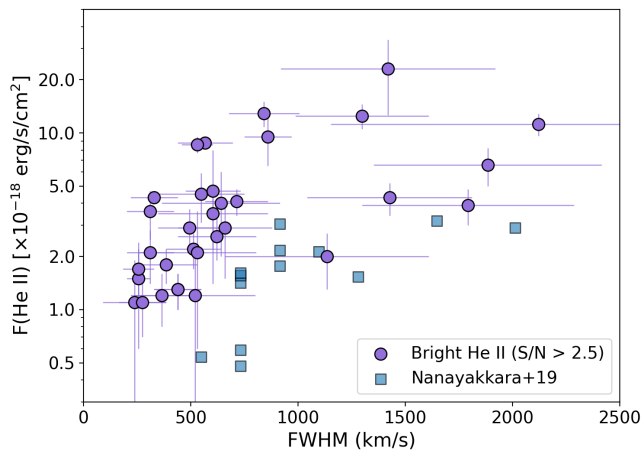


Fig. 1: Distribution of the measured He II line flux and the rest frame FWHM for *Bright* He II emitters ( $S/N > 2.5$ ) identified in both CDFS and UDS fields. Shown for comparison are line measurements of He II emitters from Nanayakkara et al. (2019) at comparable redshifts to our sample.

The He II line flux in our sample ranges from  $1.1 \times 10^{-18}$  to  $3.1 \times 10^{-17}$  erg s $^{-1}$  cm $^{-2}$ . The FWHM (rest-frame) ranges from 240 to 2120 km s $^{-1}$ . The range of EW (rest-frame) measured across galaxies in both fields ranges from 0.9 Å to 21.4 Å. The measured He II line properties for the *Bright* sources are shown in Table 1. In Figure 1 we show the distribution of the measured He II fluxes and FWHM (rest frame) for *Bright* sources, and show measurements from the Nanayakkara et al. (2019) sample, which offers the best sample to compare our He II emitters owing to its very similar redshift range. In Figure A.1 we show the *Bright* He II emitters identified in both the CDFS and UDS fields. In the following, we identify and remove possible AGNs.

### 2.3. Possible AGNs in the sample

The high ionisation potential needed for He II emission can often be achieved by AGNs and therefore it is important to identify possible AGNs that may be present in the shortlisted sample of He II emitters from VANDELS. We identify possible AGNs by searching for strong C IV emission in the spectra, similar to Nanayakkara et al. (2019). The motivation for doing this is that the ionisation potential of C $^{++}$  is high (49.9 eV) and generally the C IV emission undergoes strong absorption from stellar winds. Therefore, it is not very common for the spectra of normal star-forming galaxies to show strong C IV in emission (see Shapley et al. 2003), and more often than not, C IV emission is found in the spectra of AGNs and/or radio galaxies.

Therefore, we inspected the spectrum of all the shortlisted He II emitters (both *Bright* and *Faint*) to look for signs of C IV emission. Those galaxies that show C IV emission have been marked as likely AGNs, indicated by an asterisk in Table 1. We remove these sources from the analysis that follows in order to explore the properties of He II emission from star-formation activity alone. In Section 4.3 we explore sources that show both He II and C IV emission in more detail.

Additionally, we use the deep X-ray data available in the VANDELS field to identify X-ray AGNs in the sample. The CDFS X-ray catalogue, with  $\approx 7$  Ms of exposure time (Luo et al.

2017), is significantly deeper than the UDS catalogue with  $\approx 600$  ks of exposure time (Kocevski et al. 2018). We cross-match the RA and Dec of He II -emitting sources with the X-ray catalogues using a radius of 1 arcsecond to minimise misidentifications. We do not find any cross-matches in the CDFS field, but find two matches in the UDS field, one of which was already identified as a potential AGN due to the presence of strong C IV emission in its spectrum. X-ray-detected sources are marked with (\*) in Table 1.

### 2.4. Stacking

Since the average S/N of emission lines in individual spectra is relatively weak, we extend our analysis to also include stacks of He II emitters. In this section we describe the different classes of objects that are stacked together to boost S/N in order to aid the analysis that follows and we begin by describing the stacking procedure.

The stacking is performed by first converting each spectrum to rest-frame. Wherever accurate systemic redshifts could not be determined, for example due to faintness of the He II line in *Faint* He II emitters, we use the spectroscopic redshift determined by the VANDELS team based on template fitting of multiple emission and absorption features in the spectrum (Pentericci et al. 2018). The stacking method adopted in this study is similar to that used by Marchi et al. (2018). The rest-frame spectra are first normalised using the mean flux density value in the wavelength range 1460 – 1540 Å, and assigned a weight based on the errors on flux in this range, where a higher weight is assigned to sources with lower errors. The spectra are then re-sampled to a wavelength grid ranging from 1200 to 2000 Å, with a step size of 0.567 Å – the wavelength resolution obtained at a redshift of 3.5, which is roughly the median redshift of VANDELS sources in this study. The wavelengths that are not covered in the rest-frame spectra are masked on a source-by-source basis. We also mask residual sky lines in the spectra. The spectra are then stacked using an error-weighted averaging procedure. The  $1\sigma$  errors on the stacked spectra are calculated using bootstrapping – we randomly sample and stack the same number of galaxies from the parent sample 100 times, and the dispersion on fluxes thus obtained gives the errors.

#### 2.4.1. Faint sources

For sources classified as *Faint* He II emitters, we rely on stacking to boost the signal of the He II and other lines present in their spectra. Stacking serves as an additional check to ensure that the *Faint* sources are indeed bona fide He II emitters, which we can confirm by comparing with the stacked spectrum of all the sources in the parent sample that were not classified as He II emitters. Before stacking, we ensure that none of the sources are classified as possible AGNs.

The resulting stack of 17 *Faint* He II -emitting galaxies in the CDFS and UDS fields (black) and the stack of 899 galaxies not identified as He II emitters (red) are shown in Figure 2, with a zoom-in on the He II line shown in the inset. The presence of a narrow He II emission line is clear in the stack of galaxies classified as *Faint* He II emitters, which gives us confidence to include the *Faint* sources in the analysis that follows. There seems to be weak, possibly broad He II emission even in the stack of non-He II -emitting galaxies, which may be resulting from low-level emission present in the spectra of galaxies that we could not identify as He II emitters with a high degree of confidence.

Table 1: Measured He II line properties (rest frame) and derived physical properties of *Bright* sources in CDFS and UDS fields. Based on the width of the He II line, the sources are grouped as *Narrow* and *Broad*, with the distinction at  $\text{FWHM}(\text{He II}) = 1000 \text{ km s}^{-1}$ .

ID	RA	Dec	Flux ( $\times 10^{-18} \text{ erg s}^{-1} \text{ cm}^{-2}$ )	FWHM ( $\text{km s}^{-1}$ )	EW ( $\text{\AA}$ )	$z_{\text{sys}}$	$\log_{10}(M_{\star})$ ( $M_{\odot}$ )	$\log_{10}(\text{SFR})$ ( $M_{\odot} \text{ yr}^{-1}$ )
<i>Narrow</i>								
CDFS009705	03:32:20.9	-27:49:16.1	$2.2 \pm 0.5$	$510 \pm 130$	$1.3 \pm 0.4$	2.484	8.9	1.2
CDFS015347	03:32:13.2	-27:46:42.6	$1.3 \pm 0.7$	$240 \pm 145$	$1.9 \pm 1.3$	3.514	9.4	1.1
CDFS019872	03:32:47.9	-27:44:29.4	$1.1 \pm 0.4$	$280 \pm 110$	$1.8 \pm 0.9$	3.453	9.3	1.0
CDFS023170	03:32:37.8	-27:42:32.5	$2.8 \pm 1.5$	$455 \pm 110$	$1.1 \pm 0.6$	2.977	9.7	2.0
CDFS023215	03:32:40.7	-27:42:34.7	$4.3 \pm 0.2$	$330 \pm 110$	$4.1 \pm 2.6$	3.471	9.6	1.3
CDFS023527	03:32:18.8	-27:42:48.1	$1.5 \pm 0.9$	$260 \pm 55$	$0.9 \pm 0.4$	3.108	9.4	1.7
CDFS113062	03:32:02.6	-27:52:23.7	$4.0 \pm 2.0$	$640 \pm 275$	$1.4 \pm 0.7$	2.695	9.4	1.7
CDFS122687	03:33:00.1	-27:47:32.6	$2.9 \pm 0.8$	$495 \pm 150$	$1.0 \pm 0.4$	2.643	9.7	2.0
CDFS126819	03:31:55.7	-27:45:33.1	$9.5 \pm 3.0$	$860 \pm 110$	$8.0 \pm 2.0$	2.818	9.7	2.0
CDFS202040	03:32:02.5	-27:58:15.7	$2.6 \pm 0.7$	$620 \pm 180$	$3.7 \pm 1.9$	3.474	9.1	1.1
CDFS229681	03:31:59.4	-27:45:46.5	$1.2 \pm 0.9$	$520 \pm 280$	$1.9 \pm 1.5$	3.331	8.8	1.1
UDS004017	02:17:37.0	-05:15:15.4	$1.7 \pm 0.5$	$260 \pm 75$	$1.4 \pm 0.6$	2.389	10.0	1.6
UDS013586	02:17:52.5	-05:12:04.8	$3.1 \pm 1.9$	$335 \pm 100$	$0.6 \pm 0.4$	2.581	9.9	2.2
UDS019505	02:17:45.9	-05:10:09.1	$2.1 \pm 1.5$	$530 \pm 275$	$0.7 \pm 0.5$	2.865	9.6	1.4
UDS020089	02:17:22.7	-05:09:54.1	$2.1 \pm 0.7$	$310 \pm 110$	$2.6 \pm 1.4$	3.218	9.4	0.9
UDS021062	02:16:58.1	-05:09:35.4	$1.2 \pm 0.4$	$365 \pm 145$	$1.1 \pm 0.5$	2.537	9.6	1.8
UDS196554	02:17:40.8	-05:05:56.3	$3.5 \pm 1.3$	$600 \pm 255$	$2.4 \pm 1.3$	2.618	10.0	2.3
UDS200677	02:18:14.1	-05:04:49.2	$4.7 \pm 1.0$	$600 \pm 130$	$2.4 \pm 0.7$	3.587	9.8	2.1
UDS281893	02:17:11.3	-05:22:17.6	$2.9 \pm 1.4$	$660 \pm 220$	$1.1 \pm 0.6$	2.697	9.1	1.4
UDS292392	02:18:18.4	-05:20:41.4	$3.6 \pm 1.1$	$310 \pm 110$	$5.5 \pm 4.0$	4.555	8.9	1.2
<i>Broad</i>								
CDFS021470	03:32:21.9	-27:43:38.8	$3.9 \pm 0.9$	$1800 \pm 500$	$2.6 \pm 0.8$	2.574	9.1	1.3
CDFS102149	03:31:59.7	-27:58:02.6	$2.0 \pm 0.7$	$1130 \pm 480$	$2.0 \pm 0.9$	2.614	9.9	2.0
CDFS129134	03:31:59.0	-27:44:23.5	$11.2 \pm 1.6$	$2120 \pm 970$	$3.8 \pm 0.9$	3.202	9.6	1.8
CDFS141081	03:33:10.1	-27:40:48.2	$4.3 \pm 0.9$	$1425 \pm 385$	$3.5 \pm 1.2$	2.385	9.9	1.4
CDFS231194	03:33:02.6	-27:45:01.8	$12.5 \pm 2.0$	$1300 \pm 530$	$2.2 \pm 0.6$	3.077	9.5	1.8
UDS137388	02:17:12.2	-05:22:31.5	$23.1 \pm 10.5$	$1420 \pm 500$	$4.6 \pm 3.5$	2.598	9.6	1.9
<i>AGN</i>								
CDFS006327*	03:32:42.8	-27:51:02.6	$1.3 \pm 0.3$	$440 \pm 100$	$5.2 \pm 2.8$	3.493	8.8	1.1
CDFS028933*	03:32:07.1	-27:50:55.5	$1.3 \pm 0.3$	$440 \pm 110$	$4.7 \pm 2.1$	3.787	8.8	1.0
CDFS208098*	03:32:52.3	-27:55:26.3	$6.6 \pm 1.6$	$1885 \pm 530$	$3.5 \pm 1.4$	2.478	9.0	1.3
UDS020721 <sup>x</sup>	02:17:38.1	-05:09:47.1	$12.9 \pm 2.1$	$840 \pm 165$	$7.5 \pm 2.8$	2.520	10.7	2.1
UDS021234*	02:17:41.0	-05:09:31.3	$1.8 \pm 0.4$	$385 \pm 145$	$3.7 \pm 2.2$	4.600	9.7	0.7
UDS025482 <sup>x,*</sup>	02:17:03.4	-05:08:04.7	$4.1 \pm 0.7$	$710 \pm 145$	$4.3 \pm 1.8$	3.523	10.3	0.9
UDS145830*	02:18:13.6	-05:20:11.4	$8.6 \pm 0.9$	$530 \pm 75$	$21.4 \pm 10.6$	3.210	10.7	1.0

**Notes.** Possible AGNs have been indicated using an asterisk for those sources with strong C IV emission in their spectra, and an ‘X’ for sources with X-ray detections. Sources with ID > 100000 have ground-based photometry only. The RA and Dec are in J2000 epoch.

Nevertheless, the higher strength of He II seen in the stack of *Faint* emitters compared to the non-emitters is clear from Figure 2.

#### 2.4.2. Broad and Narrow He II emitters

To understand the underlying differences between narrow and broad He II emission lines as well as boost the overall S/N of the spectra of He II emitters, we produce stacks of sources that fall into each of these classes. Out of the *Bright* emitters, we classify sources with He II FWHM < 1000 km s<sup>-1</sup> as *Narrow*, and sources with He II FWHM > 1000 km s<sup>-1</sup> as *Broad*, in line with the analysis of Cassata et al. (2013). The physical motivation behind such a separation is the underlying mechanism that is likely powering the He II line. He II emission from evolved WR stars is expected to be broad, with FWHM ≥ 1000 km s<sup>-1</sup> (Schaerer 2003; Brinchmann et al. 2008). However, narrow

nebular He II emission is still relatively poorly understood and requires low-metallicity, high-stellar-mass populations. Therefore, to qualitatively separate out the likely WR dominated and low-metallicity populations, we separate sources based on their He II FWHM.

In Figure 3 we show the distribution of He II EWs and FWHM of our sample of *Bright* He II emitters. The dashed line marks the classification of sources as *Narrow* or *Broad*, and red circles mark the sources that show strong C IV emission and/or X-ray detections and are therefore classified as candidate AGNs. After removing seven AGNs from the analysis, we find that 20 He II emitters are classified as *Narrow* and 6 are classified as *Broad*. The resulting stacked spectra of the two classes of He II emitters are shown in Figure 4, together with the stacked spectrum of the *Faint* He II emitters. Also shown for each stack are errors obtained through bootstrapping. The num-

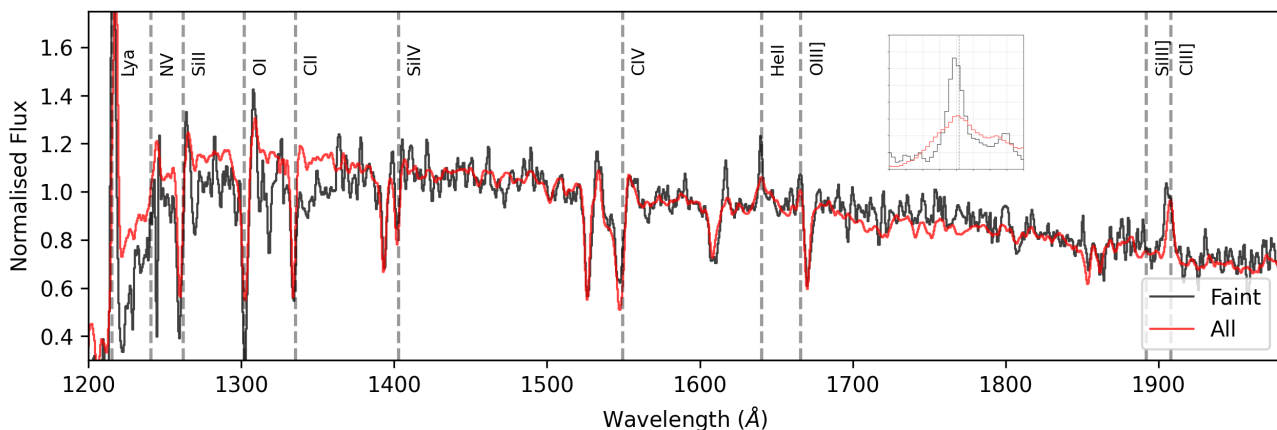


Fig. 2: Stacked spectrum of 17 *Faint* He II emitters from both CDFS and UDS fields (black) and the stack of 899 sources from the parent sample in both fields with no He II emission (red). Shown in the inset is a zoom-in of the He II line, clearly demonstrating that there is He II emission in the stack of the *Faint* emitters. This gives us confidence to include even the *Faint* emitters in this study. The errors on the *Faint* stack are shown in Figure 4.

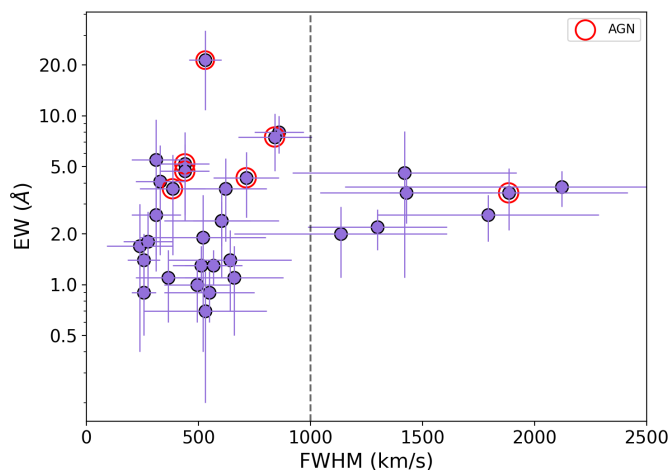


Fig. 3: Distribution of He II EW and FWHM for sources in our sample. Marked by the dashed line is the cut in FWHM = 1000 km s<sup>-1</sup> introduced to create subsamples for stacking analysis. This separation has been motivated by previously observed (and expected) He II FWHM from narrow and broad emitters – the broad He II can generally be explained by AGN and/or stellar winds, whereas narrow He II emission is generally attributed to low-metallicity stars (see Cassata et al. 2013). Sources with strong C IV emission or X-ray detection that have been tentatively classified as AGNs are excluded from further analysis, and are marked by red circles.

ber of sources that make up the stacked spectrum for each class of He II emitters is shown in Table 2.

The emission lines in these stacks are then measured by fitting a single Gaussian to the stacked spectrum. Since only line ratios are required for diagnostic plots, the normalisation of the stacked spectra is cancelled out. To capture the errors on the continuum and the subsequent errors on the line flux measurements introduced by stacking, we use the following method. We choose a region in the spectrum that is free of emission close to each line of interest, and we calculate the mean and standard deviation of

Table 2: Number of sources in each subsample used to produce stacked spectra, after removing seven AGNs from the sample.

Class	Property	No. sources
<i>Faint</i>	S/N(He II) < 2.5	17
<i>Narrow</i>	FWHM(He II) < 1000 km s <sup>-1</sup>	20
<i>Broad</i>	FWHM(He II) ≥ 1000 km s <sup>-1</sup>	6

the continuum close to the line. We then randomly sample 100 continuum values within  $\pm 1\sigma$  of the mean continuum. We then fit a Gaussian to the emission line for every continuum value determining the line flux. The median emission line flux is the median of 100 fluxes obtained using varying continuum values, and the standard deviation of the line fluxes gives the error on the flux measurement of the line.

### 3. Physical properties of He II emitters

Thanks to the availability of excellent multi-wavelength data ranging from ultraviolet (UV) to mid-infrared (MIR) from both space-based and ground-based telescopes in the VANDELS fields, it is possible to accurately derive the physical properties of sources with reliable spectroscopic redshifts. Physical parameters such as stellar masses ( $M_*$ ), dust attenuation ( $A_V$ ), star-formation rates (SFRs), and rest-frame absolute UV magnitudes ( $M_{UV}$ ) were obtained by fitting spectral energy distribution (SED) templates to photometric points from broad-band filters at the spectroscopic redshift of each galaxy. The SED fits were performed using  $Z = 0.2 Z_\odot$  metallicity versions of the standard Bruzual & Charlot (2003) models with redshifts fixed to the VANDELS spectroscopic redshift. The star-formation rates were corrected for dust using the fitted  $A_V$  value and adopting the Calzetti et al. (2000) dust attenuation law. The rest-frame magnitudes were calculated using a 200 Å wide top-hat filter centred at 1500 Å. We refer the readers to McLure et al. (2018) for full details of the SED fitting techniques, model assumptions, and derived physical parameters.

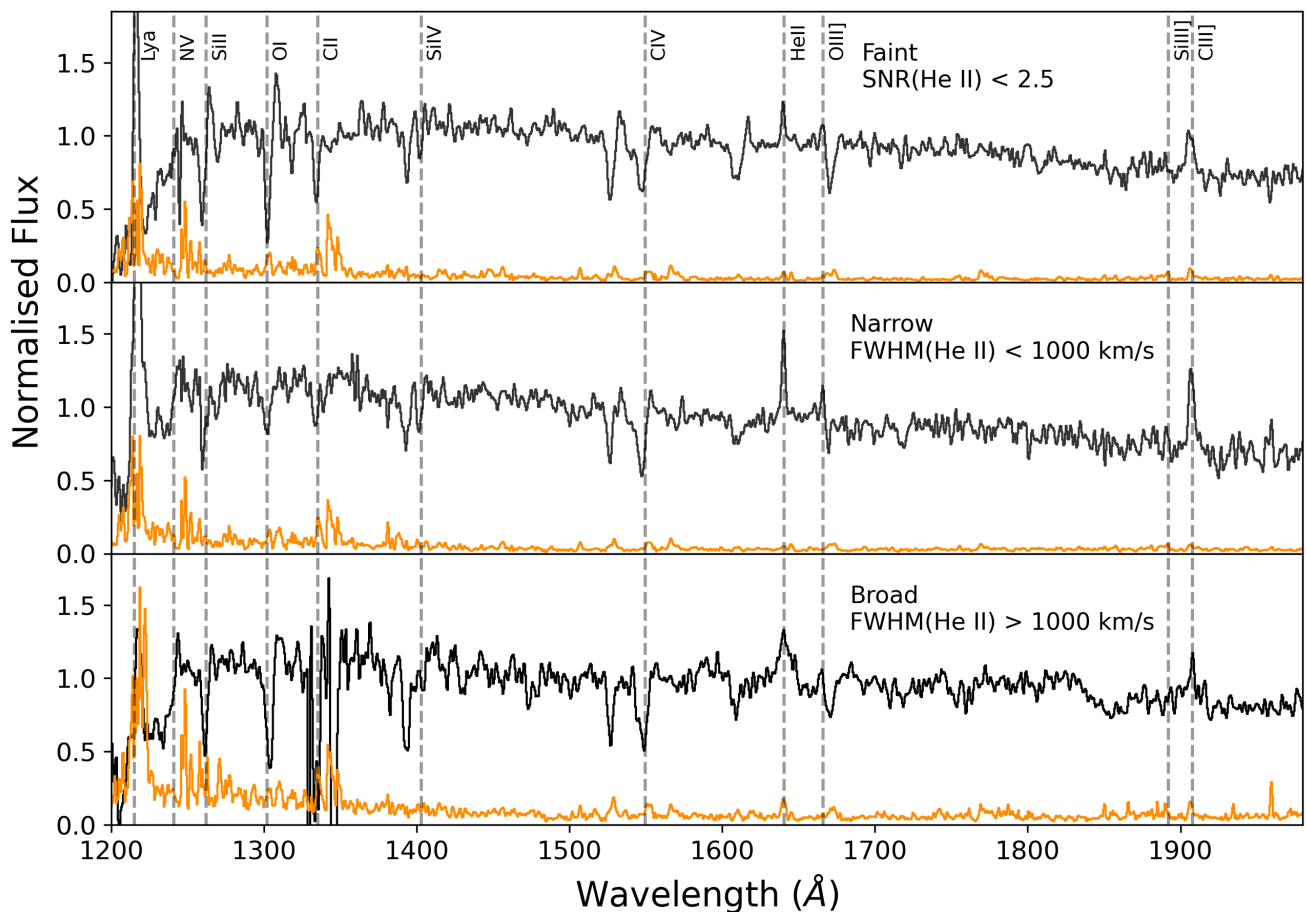


Fig. 4: Stacked spectra of sources classified as *Faint* (top), *Narrow* (middle), and *Broad* (bottom) He II emitters. There are a total of 17 sources making up the *Faint* stack, 20 sources making up the *Narrow* stack, and 6 sources making up the *Broad* stack. The errors obtained from bootstrapping are shown for each stack.

### 3.1. Stellar masses

We find that for *Bright* He II emitters in our sample, the stellar masses range from  $\log_{10} M_{\star} = 8.8 - 10.7 M_{\odot}$  and for *Faint* emitters, the stellar masses range from  $\log_{10} M_{\star} = 8.8 - 10.2 M_{\odot}$ . In the left panel of Figure 5 we show the distribution of the derived stellar masses with redshift for both *Bright* and *Faint* sources in our sample. Also shown in Figure 5 are the stellar masses and redshifts of the Parent sample.

It is clear from the figure that both *Bright* and *Faint* He II -emitting galaxies are evenly distributed across stellar mass and redshift. To quantitatively explore any differences between galaxies that show He II emission and those that do not, a two-sample Kolmogorov-Smirnov (KS) test of the stellar mass distributions of the He II emitters and the 899 galaxies with no He II emission was performed. The null hypothesis is that both samples are drawn from the same population of galaxies. The D-statistic returned by the KS test was 0.17, with a p-value of 0.29, which does not rule out the null hypothesis. Therefore, based on their stellar masses, there is no significant difference in the population of galaxies that show He II emission compared to those that do not.

For comparison, in Figure 5 we also show stellar masses from He II -emitting galaxies in the Cassata et al. (2013) sample. Our He II emitters have comparable masses to the Cassata et al. (2013) sample, although our sample extends to higher redshifts where the observed stellar masses tend to be lower, which

is due to VANDELS source selection. More details about target selection and potential biases can be found in McLure et al. (2018).

### 3.2. Star formation rates

The dust-corrected SFRs of *Bright* He II emitters are in the range  $\log_{10}(\text{SFR}) = 0.7 - 2.3 M_{\odot} \text{ yr}^{-1}$  and those of *Faint* emitters are in the range  $\log_{10}(\text{SFR}) = 0.5 - 1.9 M_{\odot} \text{ yr}^{-1}$ . We show the distribution of SFRs with redshift in the middle panel of Figure 5, with measured SFRs from the parent sample and from Cassata et al. (2013) also shown.

We do not find any significant difference between the distribution of SFRs of He II -emitting galaxies and that from galaxies with no He II emission. The distribution of SFRs are also comparable with the Cassata et al. (2013) sample, although there are a few galaxies with very high SFRs ( $\sim 1000 M_{\odot} \text{ yr}^{-1}$ ) in the Cassata et al. (2013) sample that are not present in our sample. The overall spread of SFRs in our sample is also lower than that in the Cassata et al. (2013) sample. The underlying differences in the SFR estimation through SED fitting between the two samples may add to the uncertainties in these quantities. The stellar masses and star-formation rates for *Bright* He II emitters are also shown in Table 1.



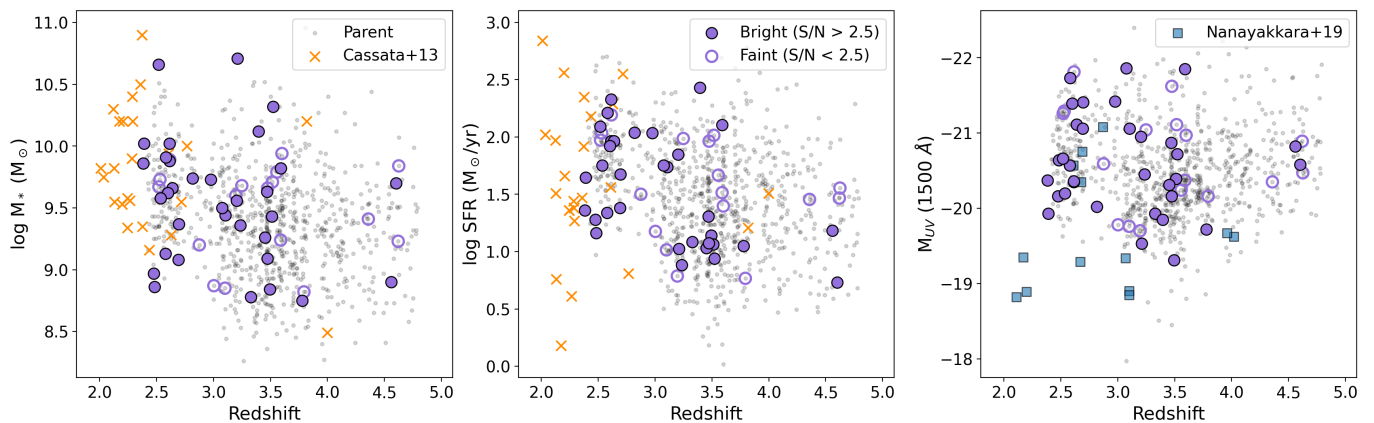


Fig. 5: Distribution of the derived stellar masses (*left*), star-formation rates (*centre*), and rest-frame UV magnitudes (*right*) of *Bright* (filled circles) and *Faint* (open circles) He II emitters with redshift. Also shown are measurements for the Parent sample (grey dots) and for He II emitters reported by Cassata et al. (2013) (orange crosses) and Nanayakkara et al. (2019) (blue squares). For our sample, we do not see any significant differences between the stellar masses, SFRs, and UV magnitudes of He II emitters and the parent sample. Our measurements are also comparable with those from the literature, although the Cassata et al. (2013) sample probes lower redshifts compared to both the Nanayakkara et al. (2019) and our He II emitters.

### 3.3. Specific SFR

We also compare the specific star-formation rates (sSFR) for He II emitters with those of the parent sample. Unsurprisingly, the distribution of sSFR for He II emitters is not significantly different from that of the parent sample. The median specific SFR for He II emitters is  $\log_{10}(\text{sSFR}) = -7.7 \text{ yr}^{-1}$  and is comparable to the values derived by Cassata et al. (2013) for their sample, although some of their galaxies show much higher sSFRs. The relatively high sSFR of our He II emitters suggests that overall, these galaxies are in the process of actively assembling their stellar masses and their stellar ages are low, assuming that they have been constantly forming stars at the same rate.

### 3.4. Rest-frame UV magnitudes

The rest-frame UV magnitudes (at 1500 Å) for *Bright* sources range from  $M_{\text{UV}} = -21.9$  to  $-19.2$ , and for *Faint* sources range from  $M_{\text{UV}} = -21.8$  to  $-19.8$ . We show the UV magnitudes with redshift for our sample, along with those from the parent sample and the sample of He II emitters reported by Nanayakkara et al. (2019).

We find He II emission originating from galaxies with a wide range of absolute UV magnitudes, all the way to the faintest limits of the survey. However, we again find no significant difference between the underlying populations of He II emitters and galaxies with no He II based on their absolute UV magnitudes. The Nanayakkara et al. (2019) sample for comparison probes fainter UV magnitudes than our sample.

Overall, we find no significant differences in the examined physical properties of galaxies that show He II emission and galaxies that do not. This is interesting as the ionisation energies required to produce bright He II emission are quite high, and why some galaxies show He II while a large majority do not is not immediately clear from the comparison above. In Section 5.1 we compare the metallicities of galaxies with He II emission and to those of galaxies without. In the following sections, we set some constraints on the underlying ionising properties of He II-emitting galaxies in a bid to understand the processes that may be driving He II emission.

## 4. Comparison with photo-ionisation models

In this section we take a deeper look at the underlying ionising mechanisms that power the observed He II emission. We carry out the analysis both on measurements made on individual spectra of *Bright* He II emitters, as well as stacks of spectra created in bins of He II FWHM. We also measure the emission line fluxes of the stack of all the *Faint* He II emitters (presented in Section 2.3).

To compare UV emission line ratios with models, we primarily rely on the He II, O III] and C III] lines given the line strengths and the wavelength coverage based on the redshift distribution of sources. We include the analysis of UV line ratios of individual sources for which the S/N of each of these emission lines is greater than 2.5, and in Table 3 we give the measured UV emission line properties for these sources.

### 4.1. Comparison with Gutkin et al. (2016)

We now compare our results with the predictions from photo-ionisation models for nebular emission from star-forming galaxies from Gutkin et al. (2016). The models make use of the latest version of the stellar population synthesis code by Bruzual & Charlot (2003) in combination with the photo-ionisation code CLOUDY (Ferland et al. 2013). The key parameters dictating the line ratios obtained from their models are the metallicity of the ISM, the ionisation parameter, the dust-to-metal mass ratio, the carbon-to-oxygen abundance ratio (C/O), the gas density of hydrogen, and the upper mass cutoff of the stellar IMF. For the purposes of our analysis, we use three different ISM metallicities:  $Z = 0.0002, 0.002$ , and  $0.02$ , where the solar metallicity is  $Z_{\odot} \approx 0.02$ . We also use two different C/O values for each metallicity:  $C/O = 0.1$  and  $0.44$ , where solar  $C/O = 0.44$  (Gutkin et al. 2016). The C/O values observed for star-forming galaxies at  $z \sim 3$  have been seen to lie within this range (see e.g. Amorfn et al. 2017). We fix the dust-to-metal mass ratio at 0.3, which is the present-day Galactic value, and the hydrogen gas density to  $100 \text{ cm}^{-3}$ , as this is the closest value available in the models to the measured typical value of  $250 \text{ cm}^{-3}$  for gas density in star-forming galaxies at high redshifts (Sanders et al. 2018). We find that there is no difference in the model outputs for  $n_H = 100$



Table 3: Ultraviolet line measurements for individual galaxies with high enough S/N for the lines.

ID	He II $\lambda 1640$			O III] $\lambda 1661 + \lambda 1666$			C III] $\lambda 1909$		
	Flux ( $\text{erg s}^{-1} \text{cm}^{-2}$ )	FWHM ( $\text{km s}^{-1}$ )	EW ( $\text{\AA}$ )	Flux ( $\text{erg s}^{-1} \text{cm}^{-2}$ )	FWHM ( $\text{km s}^{-1}$ )	EW ( $\text{\AA}$ )	Flux ( $\text{erg s}^{-1} \text{cm}^{-2}$ )	FWHM ( $\text{km s}^{-1}$ )	EW ( $\text{\AA}$ )
<i>Narrow</i>									
CDFS015374	1.1	240	1.7	$1.6 \pm 1.4$	$250 \pm 150$	$3.2 \pm 2.8$	$3.1 \pm 2.4$	$510 \pm 300$	$6.5 \pm 5.0$
CDFS023170	2.8	455	1.1	$1.3 \pm 1.1$	$315 \pm 300$	$0.7 \pm 0.6$	$6.5 \pm 2.4$	$850 \pm 150$	$3.2 \pm 0.4$
CDFS023527	1.5	260	0.9	$2.6 \pm 1.4$	$270 \pm 110$	$1.6 \pm 0.9$	$8.7 \pm 3.1$	$580 \pm 110$	$6.9 \pm 2.4$
CDFS113062	4.0	640	1.4	$2.4 \pm 1.8$	$450 \pm 225$	$0.9 \pm 0.7$	$12.3 \pm 2.2$	$630 \pm 50$	$5.6 \pm 1.0$
CDFS126819	9.5	860	8.0	$2.4 \pm 1.8$	$220 \pm 170$	$2.4 \pm 1.8$	$9.9 \pm 4.0$	$820 \pm 150$	$8.0 \pm 3.2$
UDS013586	3.1	335	0.6	$2.8 \pm 2.4$	$400 \pm 130$	$0.6 \pm 0.5$	$12.0 \pm 3.1$	$800 \pm 100$	$3.3 \pm 0.8$
UDS019505	2.0	530	0.7	$2.2 \pm 2.0$	$420 \pm 140$	$0.9 \pm 0.8$	$8.3 \pm 2.4$	$860 \pm 120$	$4.5 \pm 1.3$
UDS281893	2.9	660	1.1	$2.1 \pm 1.1$	$450 \pm 70$	$0.9 \pm 0.5$	$7.1 \pm 1.3$	$600 \pm 60$	$4.1 \pm 0.2$
CDFS009705	2.2	510	1.3	-	-	-	$8.6 \pm 1.1$	$820 \pm 50$	$6.3 \pm 0.8$
CDFS229681	1.2	520	1.9	-	-	-	$3.9 \pm 2.7$	$600 \pm 290$	$8.6 \pm 6.0$
<i>Broad</i>									
UDS137388	23.1	1420	4.6	-	-	-	$16.0 \pm 6.3$	$1100 \pm 280$	$5.0 \pm 2.0$

**Notes.** Line fluxes are in units of  $10^{-18} \text{ erg s}^{-1} \text{ cm}^{-2}$ . The O III] FWHM given in the table is for the  $\lambda 1666$  line. The errors on He II line properties are given in Table 1.

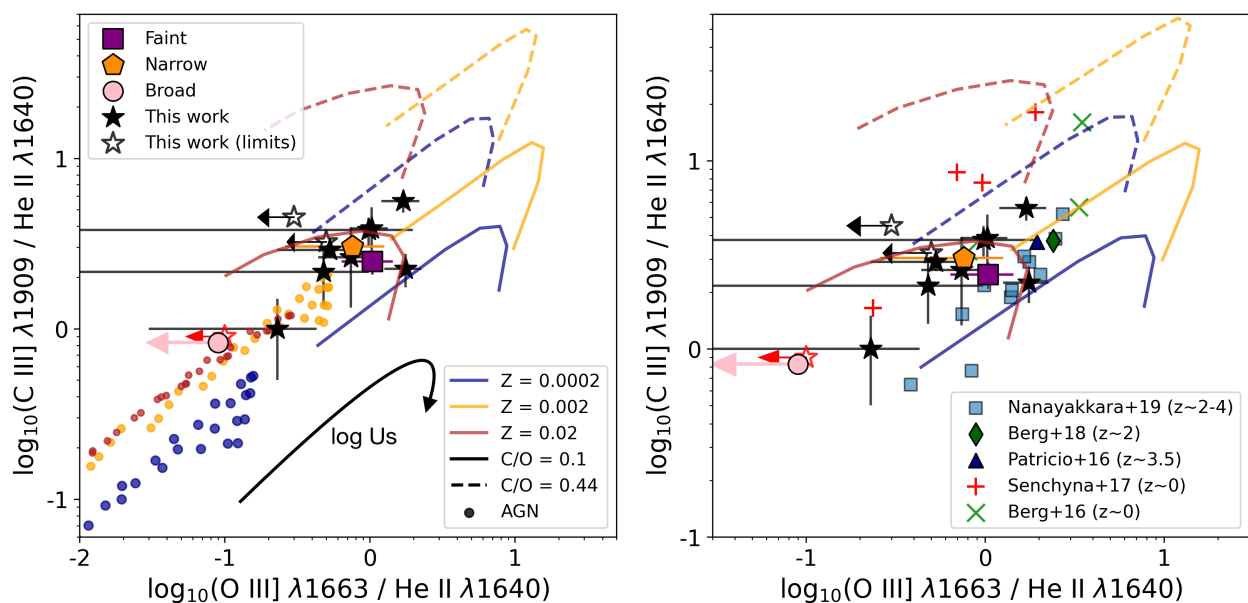


Fig. 6: *Left:* UV line ratios determined for individual galaxies (stars, where empty stars are limits) and stacks of He II emitters (coloured symbols), compared with photo-ionisation models from star-forming galaxies (lines) by Gutkin et al. (2016) and AGNs (dots) by Feltre et al. (2016). The red star indicates limits on a broad He II -emitting galaxy. Both models for star-formation and AGNs are shown for three metallicities:  $Z = 0.0002, 0.002$  and  $0.02$ . For star-formation models, the solid lines indicate  $C/O = 0.1$ , and the dashed lines indicate  $C/O = 0.44$  (solar value). *Right:* Zoom in on the star-forming region with AGN models removed for clarity. We also show line ratios from the sample of He II emitters of Nanayakkara et al. (2019). Also shown are measurements from local low-metallicity galaxies from Senchyna et al. (2017) and Berg et al. (2016), and individual lensed galaxies at  $z = 2.2$  (Berg et al. 2018) and  $z = 3.5$  (Patricio et al. 2016). Line ratios of individually detected galaxies from our sample, as well as stacks of *Faint* and *Narrow* He II emitters favour the star-forming models, whereas the stack of *Broad* emitters occupies a region between the star-forming and AGN models. The separation between narrow and broad emitters suggests that they are probably powered by different ionising mechanisms and/or conditions.

$\text{cm}^{-3}$  or  $250 \text{ cm}^{-3}$ . We use an upper mass cutoff of  $300 M_{\odot}$  so as to capture the contribution from the most massive stars. The predicted line ratios from the model are a result of constant star formation at a rate of  $1 M_{\odot} \text{ yr}^{-1}$  for 100 Myr. The dimensionless ionisation parameter ( $U_s$ ), which is the ratio of the ionising photon flux and the gas density (see Kewley et al. 2019, for a detailed explanation), is left free for each track.

This analysis is focused on the diagnostic that uses the line ratios O III] / He II versus C III] / He II. For O III] flux, we sum the contributions of the O III]  $\lambda 1661$  and  $\lambda 1666$  lines. There are eight galaxies in our sample that have enough SNR for all three lines to enable a reliable individual line ratio measurement. Additionally, there are three He II -emitting galaxies with detections of C III] only, and for these we use limits on O III]. We also analyse

the line ratios determined from the stacked spectra of the different classes of He II emitters mentioned earlier. In Figure 6 we show the measured line ratios of individual sources and stacks, with the star-formation models from Gutkin et al. (2016) ranging in ionisation parameter values,  $-4 < \log U_s < -1$ , and AGN models from Feltre et al. (2016) ranging within  $-5 < \log U_s < -1$ . The AGN models have a gas density  $n_H = 1000 \text{ cm}^{-3}$  for AGNs with a dust-to-metal ratio of  $\xi_d = 0.3$ . We find that using other (fiducial) values of  $n_H$  or  $\xi_d$  does not have a major impact on the parameter space occupied by AGNs. Models for three different metallicities are used:  $Z = 0.0002, 0.002$ , and  $0.02$ . The value of the ionisation parameter for each model ( $\log U_s$ ) increases from the bottom left towards the top right in the Figure 6.

Given the weak line strengths of other UV lines observed in individual galaxy spectra, a quantitative analysis performed using chi-squared minimisation is beyond the scope of this work. However, we provide some qualitative constraints on the ionising source properties of He II -emitting galaxies based on the model predictions. Additionally, to put into context the properties of our sample of He II emitters, we also compare our line ratios with galaxies that have similar properties in the literature. Figure 6 shows that the UV line ratios of the majority of individual He II emitters favour ionisation from star formation as opposed to AGNs. There are degeneracies between the model metallicities that can reproduce the line ratios. The subsolar metallicities with C/O ratios between 0.1 and 0.38 require lower ionisation parameter values in the range  $-3 < \log U_s < -2$  to reproduce the line ratios, whereas solar metallicity models require  $\log U_s > -2$  to reproduce the observed line ratios. This degeneracy is primarily linked to the trade-off between the shape of the ionising radiation field and the number of ionising photons produced. Compared to higher metallicity populations, lower metallicities give rise to harder ionisation fields, which means that comparatively lower ionisation parameter values can still produce enough energetic ionised photons to deposit the required amount of total kinetic energy in the gas to explain the line ratios that we see in our sample.

The line ratios from stacks of both *Faint* and *Narrow* He II emitters overlap with those observed in individual galaxies with narrow He II favouring ionisation by star formation. However, the line ratios from the *Broad* stack are hard to explain using star-formation alone and favour photo-ionisation by AGNs with solar to mildly subsolar metallicities. The O III] line strength in the stack of *Broad* emitters is weak, and therefore we can only set a limit on the O III] / He II ratio. The clear separation between the *Narrow* and *Broad* He II emitters illustrates the possible differences in ionising mechanisms that power the He II emission in each case.

Figure 6 also shows line ratios from the sample of He II emitters from MUSE presented by Nanayakkara et al. (2019); this sample overlaps well with our sample in terms of redshift distribution ( $z \sim 2 - 4.5$ ) and offers the best sample for a direct comparison. We also show line ratios from individual low-mass, low-metallicity lensed galaxies at  $z = 2.2$  (Berg et al. 2018) and at  $z = 3.5$  (Patrício et al. 2016) that show extreme UV-ionising spectra, representing the conditions likely to be prevalent in galaxies that reionised the Universe at  $z > 6$ . There is considerable overlap between the line ratios of our sample and those determined by Nanayakkara et al. (2019), and measurements from lensed galaxies at  $z \sim 2 - 3$  are also similar to those seen in our He II emitters.

Additionally, we show line ratios observed in local metal-poor He II -emitting galaxies from Senchyna et al. (2017) and

Berg et al. (2016). From both these local samples we select only those sources with reliable measurements of all three emission lines in question. The  $z \sim 0$  low-metallicity galaxies have slightly higher C III] / He II ratios, but comparable O III] / He II ratios to our sample, which may be explained by higher C/O ratios in the local Universe compared to high redshifts. Line ratios of  $z \sim 0$  galaxies considered in this study also tend to favour higher stellar metallicities, which could explain the higher C/O ratios in local galaxies as C/O for star-forming galaxies has been found to be linked to the O/H ratio (Amorín et al. 2017). However, there are degeneracies between metallicity and C/O from the models, and the dominant effect that results in slightly differing line ratios between local galaxies and our sample is not entirely clear.

#### 4.2. Comparison with Xiao et al. (2018) – Binary stellar population

We now compare the UV line ratios of our galaxies and stacks with predictions from the Binary Population and Spectral Synthesis Code (BPASS; Eldridge et al. 2017; Stanway & Eldridge 2018), which are presented in Xiao et al. (2018). Since very high effective temperatures and hard ionising spectra in galaxies are required to power the nebular He II emission line, the inclusion of interacting binary stars in stellar population synthesis models may hold the key (Eldridge et al. 2017; Götzberg et al. 2018; Xiao et al. 2018; Götzberg et al. 2019). The inclusion of binary evolution in the modelling of stellar populations allows the contribution of a harder UV-ionising spectrum with a longer duty cycle to be captured (Eldridge et al. 2017).

For comparison with the predicted UV line ratios, we once again use O III] / He II versus C III] / He II from the Xiao et al. (2018) models, analysing individual galaxy spectra as well as stacks. We also again set the hydrogen gas density,  $n_H$ , to  $100 \text{ cm}^{-2}$ , and choose ISM metallicities of  $Z = 0.0001, 0.002$ , and  $0.02$ . The Xiao et al. (2018) models evolve as a single instantaneous starburst with ages varying from 1 Myr to 10 Gyr, and for this analysis we select models with stellar ages,  $10^6, 10^7$ , and  $10^8$  years. The C/O ratio in these models is fixed to the solar value of C/O = 0.44. The resulting line ratios predicted by the models as well as those measured in individual galaxies and stacks are shown in Figure 7. For each model, the ionisation parameter ranges  $-3.5 < \log U_s < -1.5$  and increases from the bottom left to the top right of the figure, as indicated by the black arrow.

The binary models from Xiao et al. (2018) seem to fit the observed line ratios more consistently with respect to degeneracies within model predictions of different metallicities, both for individual galaxies and stacks. For example, the majority of individual detections as well as the *Faint* and *Narrow* stacks favour subsolar metallicities in the range  $Z = 0.0001 - 0.002$ , with ionisation parameter  $\log U_s > -2$  and stellar ages of  $10^8$  years. Interestingly, binary stellar models suggest that the line ratios observed in *Broad* He II emitters can be explained purely by star formation and favour higher metallicities compared to the narrow emitters. A star-formation explanation is in contrast to the predictions from single-star models from Gutkin et al. (2016), where additional ionising photons from AGNs were required to explain the line ratios. The fact that *Broad* He II emitters can be explained by higher metallicity models is consistent with the picture where WR stars, predominantly formed at higher metallicities, are the dominant sources of *Broad* He II seen in spectra of star-forming galaxies. Due to binary interactions implemented in the Xiao et al. (2018) models, stars can spend a longer amount of

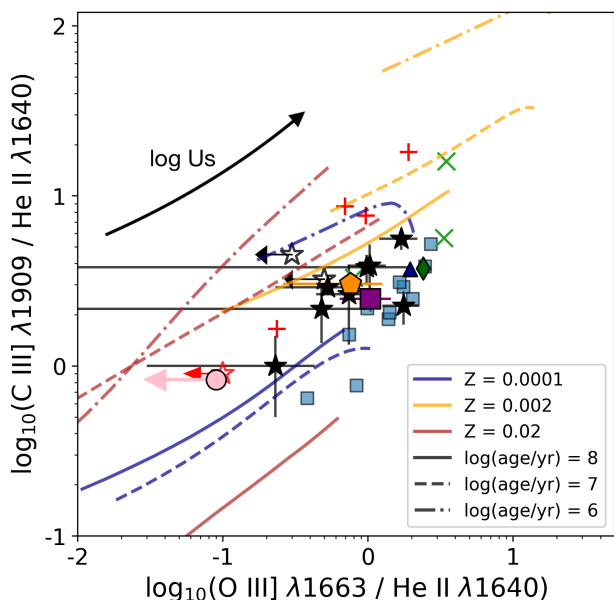


Fig. 7: UV line ratios determined for individual galaxies and stacks of He II emitters. The symbols are the same as in Figure 6. The line ratios are compared with photo-ionisation models from star-forming galaxies including binary stars from Xiao et al. (2018) with three metallicities,  $Z = 0.0001, 0.002$ , and  $0.02$ , and stellar ages  $10^6$  (dot-dashed),  $10^7$  (dashed), and  $10^8$  (solid) years. Also shown are line ratios from Nanayakkara et al. (2019), Senchyna et al. (2017), Berg et al. (2016), Berg et al. (2018), and Patrício et al. (2016) for comparison, represented by the same coloured symbols as in Figure 6. The majority of individual detections and stacks of *Narrow* and *Faint* He II emitters favour subsolar metallicities and  $\log U_s > -2$ , whereas the *Broad* emitters favour solar metallicities and lower  $\log U_s$  values.

time in the WR phase, thereby providing the required He II ionising photons for prolonged periods (Eldridge et al. 2017).

As a more direct test of whether the BPASS models can fully account for the number of He<sup>+</sup> photons produced in the sources presented in this paper, we now compare the measured and predicted EWs of the three UV emission lines in this section.

In Figure 8, we show the distribution of He II, C III], and O III] EWs from individual measurements as well as stacks, along with the predictions from Xiao et al. (2018) models for the same ages and parameters as before. We note that for individual sources, we only show the detections and not limits on measured EWs. Also shown for comparison are EW measurements from Nanayakkara et al. (2019). We find that He II emitters in our sample have similar He II, O III], and C III] EWs to those in the (Nanayakkara et al. 2019) sample. Overall, the stacks show lower O III] EWs compared to individual detections, which is not surprising as the stacks contain multiple sources that do not show strong O III] .

The Xiao et al. (2018) models with a metallicity of  $Z = 0.002$  and low stellar ages ( $10^6 - 10^7$  years) can reproduce the observed C III] EWs, which is consistent with the photo-ionisation modelling from Nakajima et al. (2018), but they fall short of reproducing the He II EWs for both individual sources and stacks. We find that the highest He II EWs are predicted by the lowest metallicity ( $Z = 0.0001$ ) models with stellar ages in the range  $10^6 - 10^7$  years, but at this metallicity the observed C III] EWs are only re-

produced by models with a stellar age of  $\sim 10^6$  years. However, these models cannot reproduce the observed O III] EWs for individual sources, but the EWs measured in the stacked spectra can be explained by models with metallicities  $Z = 0.0001 - 0.002$ . Solar metallicity models ( $Z = 0.02$ ) underpredict the EWs for all the UV lines considered by more than two orders of magnitude, effectively ruling out a solar metallicity stellar population origin of these lines.

Therefore, we conclude that the BPASS models can reproduce the observed UV line ratios but not line strengths, similar to what was reported by Nanayakkara et al. (2019). These latter authors showed that even after calibrating for the C III] deficit between observations and models, the BPASS models still underpredict the number of He II ionising photons by almost an order of magnitude. However, the very low metallicity models from BPASS come close to reproducing the observed He II EWs after applying the calibration. From our results and those of Nanayakkara et al. (2019), it is clear that additional sources that produce He II ionising photons are required to properly account for the observations. Recently, stripped stars (Götberg et al. 2018, 2019) and X-ray binaries (Schaerer et al. 2019) were suggested as extra contributors of He II ionising photons that could potentially bridge the gap left by stellar population synthesis models in order to reproduce the He II line strengths. We explore these possibilities in more detail in the following section.

#### 4.3. Revisiting the He II emitters with strong C IV

In the initial classification of sources, we used the presence of C IV emission in galaxy spectra as an indicator of AGN activity. The ionising potential required for the C IV emission line is very high ( $\sim 49.9$  eV) and close to the He II ionising potential. Therefore, standard stellar population models based on single stars are unable to reproduce strong C IV lines without including a contribution from AGNs. However, low-metallicity binary star models are capable of producing He II ionising photons (and therefore, C IV ionising photons) for longer periods of time, and therefore we revisit the spectra of sources that show C IV emission and use the BPASS models to probe their underlying ionising mechanisms.

In this analysis, we only select those galaxies that do not have an X-ray counterpart in the available catalogues and are therefore not clearly AGNs. Using BPASS model predictions, we find that the line ratios C IV / He II versus C III] / He II observed for our He II emitting galaxies with strong C IV emission can be explained using star-formation activity alone, as shown in Figure 9. The best-fitting models are those with subsolar metallicities ( $0.0001 - 0.002$ ) and stellar ages in the range  $10^7 - 10^8$  yr. We note that one C IV emitter does not show any C III] emission, and therefore a higher metallicity for this particular source cannot be categorically ruled out based on the model predictions. The models shown here are the same as Figure 7. We note that this analysis does not include the source UDS021234 as the C III] line is not covered in the observed spectrum because of its high redshift.

Several other studies have reported the detection of both C IV and He II emission in low-metallicity galaxies, predominantly in the local Universe. In the Berg et al. (2016) sample of local dwarf galaxies, three He II emitters show strong double-peaked C IV emission. Recently, Senchyna et al. (2019a) found one of the most prominent nebular C IV doublets in a local extremely low-metallicity galaxy, and show that C IV emission may be ubiquitous in extremely metal-poor galaxies with very high specific star formation rates. This is also expected, for example,

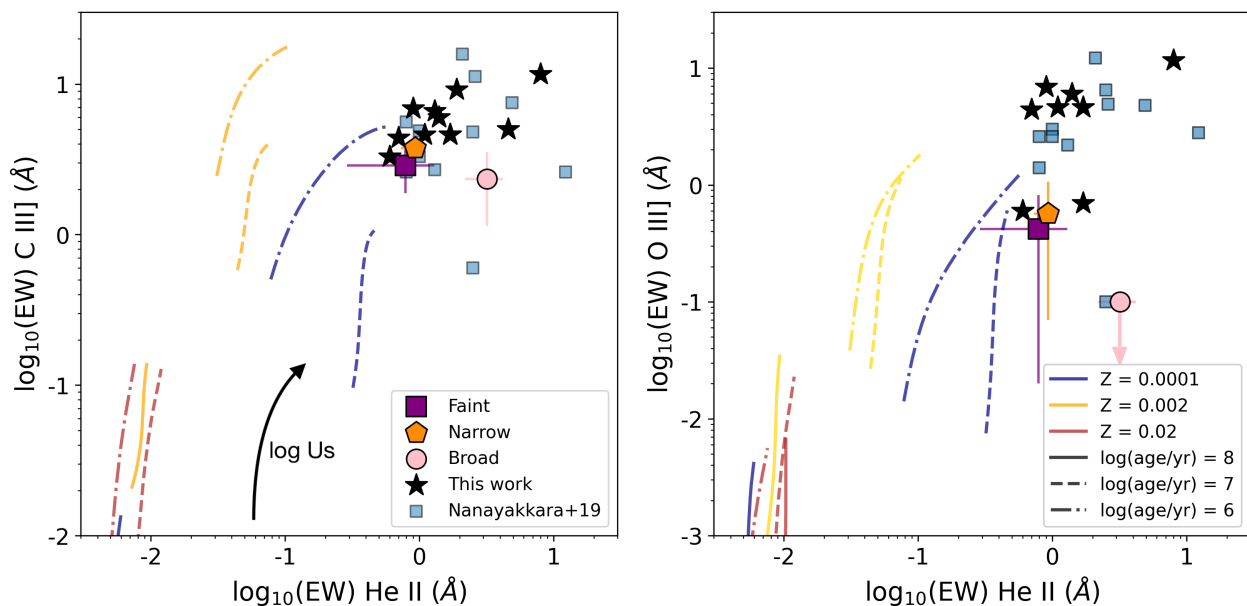


Fig. 8: Comparison of EWs measured in individual galaxies (black stars) and stacks (coloured symbols) with predictions from BPASS models. The left panel shows EWs of He II and C III], and the right panel shows EWs of He II and O III]. Also shown are EW measurements from Nanayakkara et al. (2019). The measurements from individual sources in our sample are in close agreement with those of Nanayakkara et al. (2019). The BPASS models underpredict the He II EW, but subsolar metallicity models can reproduce the C III] EW. The O III] EWs are also underpredicted at all metallicities for the majority of sources. Solar metallicity models underpredict the EWs by several orders of magnitude, and therefore we can conclude that based on the observed UV line EWs, He II -emitting galaxies tend to favour subsolar metallicities. To properly account for the missing He II ionising photons, additional mechanisms such as stripped stars (Götberg et al. 2018, 2019) or X-ray binaries (Schaerer et al. 2019) may be needed.

from photo-ionisation models of Nakajima et al. (2018). Berg et al. (2019) also reported the detection of the C IV doublet from two  $z \sim 0$  He II -emitting galaxies, and show that the presence of C IV emission may indicate both the production and the transmission of very high-energy ionising photons. The common property observed in galaxies that show both He II and C IV emission is that they tend to be low-metallicity star-forming galaxies, which is also apparent from our sources.

The presence of both He II and the resonantly scattered C IV emission lines suggests that a significant number of high-energy ionising photons with energies greater than  $\sim 49.9$  eV are being produced and transmitted (Berg et al. 2019). The escape of such high-energy photons in significant amounts is needed from low-mass star-forming galaxies at  $z > 6$  to drive the process of reionisation, and galaxies with similar properties at intermediate redshifts ( $z \sim 2 - 5$ ) as well as dwarf galaxies in the local Universe can serve as analogues to explore the physical conditions prevalent in galaxies that are expected to reionise the Universe at early times.

#### 4.4. Effects of different stellar population parameters

In this section we briefly outline what impact is seen on the line ratios and inferred physical properties by changing certain adjustable parameters that go into the stellar population synthesis modelling.

##### (i) Star-formation history

An important difference between the Gutkin et al. (2016) single-star models and Xiao et al. (2018) binary-star models is the assumed star formation history (SFH). The Gutkin et al. (2016) models assume a constant star formation rate of

$1 M_{\odot} \text{ yr}^{-1}$  for 100 Myr, whereas the Xiao et al. (2018) BPASS models assume instantaneous star formation at a given time in the galaxy’s evolutionary history. As Gutkin et al. (2016) note, in their single-star models, most ionising photons are released during the first 10 Myr of stellar evolution. This is a relatively short timescale compared to the lifetime of a galaxy and therefore it is close to quasi-instantaneous star formation, similar to what is assumed in the implementation of the BPASS models.

Eldridge et al. (2017) showed that at low stellar ages, the BPASS binary-star models produce very similar outputs to the Bruzual & Charlot (2003) model on which the Gutkin et al. (2016) models are based. The difference between the two models is especially not large at rest-frame UV wavelengths, where the light is dominated by young stars. The difference between star-formation histories is larger at redder wavelengths, where the SED is dominated by older stars. Since we are primarily interested in the UV line ratio predictions, the differences arising from assumed star-formation histories are kept to a minimum. In the context of this study, if the BPASS models also assumed a constant star formation rate for a set period of time, the galaxy ages that best fit the UV line ratios may be higher than what an instantaneous star formation history would suggest.

##### (ii) Carbon-to-oxygen abundance ratio (C/O)

For the single star models used in this analysis, we show model outputs for two C/O ratios: 0.44 (solar) and 0.1 (subsolar). For the binary models, the C/O is fixed to the solar value of 0.44. As Gutkin et al. (2016) showed, and as is also visible from the model outputs shown in Figure 6, the greatest impact of choosing a higher C/O value is an increase in the predicted C III] / He II, C III] / O III], and C IV / He II ratios. Amorín et al. (2017) showed that the C/O ratios in star-forming galaxies at  $z \sim 2 - 3$  are subsolar. This means that implementing sub-



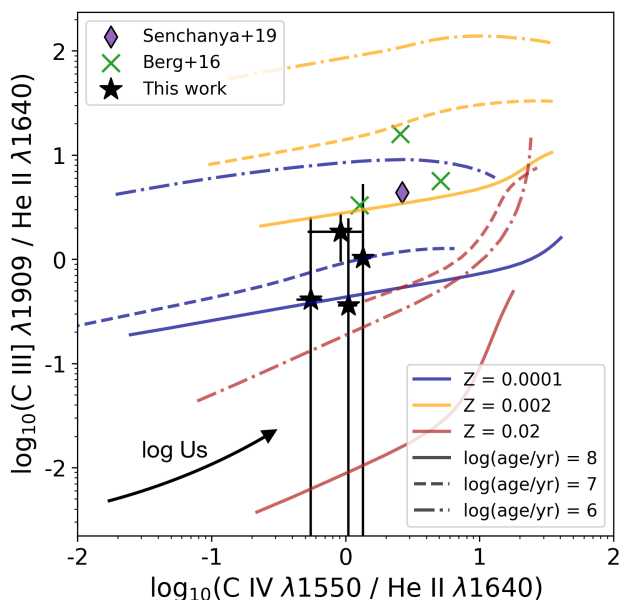


Fig. 9: Line ratios of He II-emitting galaxies that show strong C IV emission in their spectrum. Model predictions from BPASS are shown, which are able to reproduce the observed line ratios using star-formation activity alone. Also shown for comparison are line ratios measured in local low-metallicity galaxies by Berg et al. (2016) and Senchyna et al. (2019a). When compared to the local galaxies, our sources at higher redshifts favour lower metallicities.

solar C/O ratios in the Xiao et al. (2018) binary models would decrease the predicted C III] / He II ratios in Figure 7. This would affect the stellar age of models that would then best fit the observed UV line ratios. For example, for models with a stellar metallicity of  $Z = 0.002$ , younger stellar ages would be able to explain the observed line ratios in our sample of He II emitters.

### (iii) Dust-to-metal mass ratio ( $\xi_d$ )

Studies show that  $\xi_d$  is expected to vary with redshift, and is closely related to the ISM metallicity of a galaxy. It is expected that at higher redshifts and at lower ISM metallicities,  $\xi_d$  decreases (Inoue 2003; Li et al. 2019). As dust grains are made from metals injected into the ISM by stars, lower metallicities result in less dust production. Therefore,  $\xi_d$  can have an additional impact on the observed emission line ratios predicted by models. However, for simplicity, most studies generally assume a fixed  $\xi_d = 0.3$ , the Galactic value.

Gutkin et al. (2016) showed that the choice of  $\xi_d$  from 0.1 to 0.5 at lower ISM metallicities has a negligible impact on the C III] / He II, O III] / He II, and C III] / O III] ratios primarily used in this paper. The difference is also relatively minor at solar metallicity, the highest metallicity considered in this study. Therefore, we can conclude that for the metallicities considered in this paper, variation in the value of  $\xi_d$  does not result in significant differences in the predicted UV line ratios.

## 5. Discussion

In this section we put the He II emitting galaxies presented in this paper in the context of the general galaxy population at these redshifts. In particular, we look at the physical conditions that lead to production of He II in emission. We also present possible scenarios that may lead to the emergence of strong He II at high

redshifts, and what these observations mean for galaxies at even higher redshifts, a regime that the *James Webb Space Telescope* (JWST) will probe.

### 5.1. Do He II-emitting galaxies have systematically lower metallicities?

One of the requirements for He II emission from star-forming galaxies at any redshift is the presence of a young (Bergeron et al. 1997), low-metallicity (subsolar) stellar population that is capable of producing enough He II ionising photons (see e.g. Schaerer 2003). Ultraviolet spectra of several low-metallicity dwarf galaxies in the local Universe show strong He II 1640 Å emission (Berg et al. 2016, 2019; Senchyna et al. 2017, 2019a). Nanayakkara et al. (2019) showed that the UV line ratios of their sample of He II emitters at  $z \sim 2 - 4$  are also best explained by subsolar metallicity models.

Using the predictions of line ratios and the EWs of several UV emission lines from the BPASS models presented in the previous section, it is clear that our He II-emitting sources also favour subsolar metallicity (Figures 7 and 8). Although there are degeneracies between the different parameters of the models, it is clear that solar metallicities may be ruled out.

To quantitatively measure stellar metallicities of He II-emitting galaxies, we must rely on stacks that boost the S/N of key features in the spectra. To ensure sufficiently high S/N, we stack a total of 43 sources, previously classified as both ‘Bright’ and ‘Faint’ He II emitters (removing possible AGNs). The metallicities are then measured following the method of Cullen et al. (2019), which relies on a combination of stellar population synthesis modelling and metallicity indicators in the UV. With the low S/N of individual galaxy spectra, accurate metallicities using this method can only be obtained for stacks of objects. A slight caveat of the stellar metallicity measurement method from Cullen et al. (2019) used in this paper is that the SED fitting assumes a constant star-formation history. This assumption is valid for averaging across the general star-forming galaxy population, but if galaxies with He II emission are very young, then their true metallicities may be higher than what is inferred using this method.

For the stacked spectrum of all He II emitters, we measure a stellar metallicity,  $Z = 0.0022 \pm 0.0003$ , which is roughly 10% of solar metallicity. We note that the uncertainties are likely to be underestimated due to other systematic errors that are not taken into account. The metallicity is consistent with what the UV line ratio diagnostic plots suggested for the large majority of individual He II emitters and the stacks of *Faint* and *Narrow* emitters. To compare with galaxies that do not show He II emission, we randomly sample 43 spectra, the same number of sources that go into the stack of all He II emitters, from the 849 galaxies with no He II emission and stack their spectra. Choosing a comparable sample size results in comparable errors on the two stacks, which is essential for consistent metallicity determination. We also ensure that the spectra that are sampled have comparable stellar masses, SFRs, and redshifts to those with He II emission.

The metallicity that we measure for the stack of galaxies with no He II is  $Z = 0.0020 \pm 0.0002$ , and is consistent within the error bars with the stellar metallicity of He II emitters. The best-fitting templates that are used to determine metallicities for the stacks of both He II emitters and non-emitters are shown in Fig 10. Similar to our result, Steidel et al. (2016) and Topping et al. (2019) also found that models with stellar metallicities of  $0.1Z_{\odot}$  provide the best match for their sample of star-forming

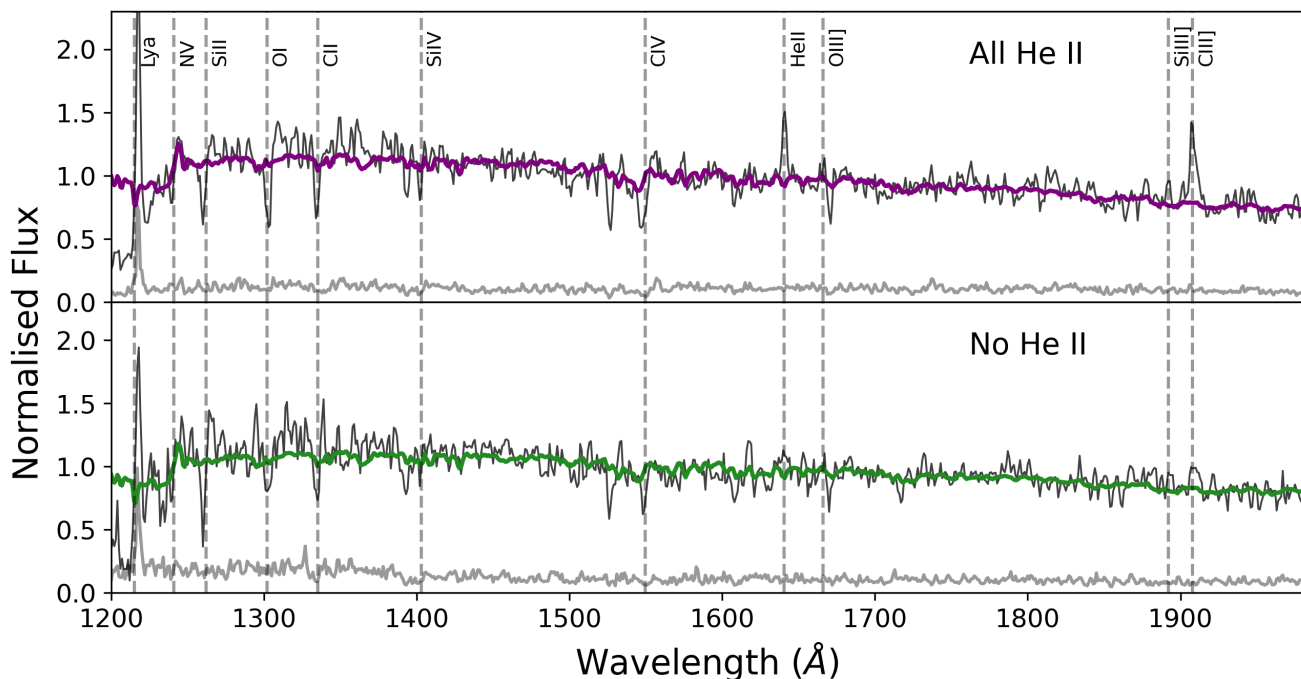


Fig. 10: Best-fitting templates using the method of Cullen et al. (2019) to determine the stellar metallicities from stacked spectra (shown in black, with errors in grey) of He II emitters (*top*) and non-emitters (*bottom*). The metallicities derived for both classes of objects are highly comparable, at roughly 10% that of solar metallicity. The inferred UV slope and fitted absorption features are comparable in both stacks, however the stack of He II emitters has stronger emission lines compared to the stack of non-He II emitters.

galaxies, although their sample lies at slightly lower redshifts ( $z \sim 2.4$ ) compared to our sample. Interestingly, our metallicity measurements show that although He II -emitting galaxies have low metallicities, they do not have significantly lower metallicities than the general star-forming galaxy population at the same redshifts. Comparable metallicities between He II emitters and non-emitters are indeed consistent with the other findings of this paper, where their derived physical properties (such as stellar mass, SFRs, rest-frame UV magnitudes, etc.) are not significantly different either. Therefore, from these results it is not immediately clear what causes only a small fraction of galaxies to show He II emission. The UV continuum slope and absorption features visible in the two stacked spectra are also comparable, with the only difference being the presence of stronger UV emission lines in the stack of He II emitters. We measure the UV slope,  $\beta$ , from the stacked spectra, where  $F_{\lambda} \propto \lambda^{\beta}$ , and find  $\beta = -0.32$  for the stack of He II emitters and  $\beta = -0.30$  for the stack of non-emitters. The UV slope is shaped by the metallicity, age, and dust properties of the underlying stellar populations, and the fact that He II emitters and non-emitters have very similar  $\beta$  values reinforces the idea that the prevalent physical conditions in these two classes of galaxies are consistent.

Nebular He II emission is most likely caused by ionisation due to massive stars residing within young stellar populations in galaxies. It has been shown that a combination of low-metallicity stellar populations, which contribute to the rest-frame UV optical lines, and a more evolved stellar population dominating the continuum emission can be used to explain the line ratios and SEDs of high-redshift galaxies (see e.g. Sobral et al. 2015). One possible way to describe the presence of He II in some galaxies is that this emission (and other strong UV lines seen in the stacked spectrum) may be the result of a recent, extreme star-formation event in the galaxy. As a result, the bright UV emission lines in

the stacked spectrum of He II emitters, originating from young and massive stars (some possibly affected by interactions in binary systems), are superimposed on a more regular stellar continuum originating from the rest of the stars in the galaxy, which dominate the bulk of the stellar mass. As mentioned earlier, a caveat of the method used to estimate stellar metallicities means that if He II -emitting galaxies indeed have young ages, then the measured metallicities will be biased. A direct probe for evidence of recent star-formation could be the H $\alpha$  emission line, and upcoming facilities such as the *JWST* and *E-ELT* will be instrumental in pioneering near-infrared spectroscopic studies of such faint galaxies.

## 5.2. Alternative sources of He II ionising photons

In the following sections we briefly explore additional physical phenomena that could give rise to He II emission in star-forming galaxies and have not yet been necessarily included in the stellar population synthesis models.

### 5.2.1. X-ray binaries

The difference between the He II EWs predicted by stellar populations that include binary stars and the EWs that we observe in our sample suggests that there may be some additional mechanisms that could account for the missing He<sup>+</sup> ionising photons. X-ray binaries (XRBs) have been suggested as one such mechanism for several decades now (see Garnett et al. 1991, for example). Schaerer et al. (2019) showed that XRB populations in low-metallicity galaxies can account for the He II line strength, and Fornasini et al. (2019) recently showed that the contribution from XRBs indeed increases with decreasing metallicities at high redshifts, as was already shown for low-redshift galaxies

(Douna et al. 2015; Brorby et al. 2016). Therefore, it is important to explore the role of XRBs in low-metallicity, He II -emitting galaxies.

One of the VANDELS fields, the Chandra Deep Field South (CDFS), has the deepest X-ray data available, with an effective exposure time of 7 Ms. In a follow-up paper (Saxena et al. in prep), we will explore the X-ray properties of individual He II -emitting sources in the CDFS that were identified in this paper, in addition to a stacking analysis of both He II emitters and non-emitters with comparable physical properties. In combination with the latest models (Schaerer et al. 2019; Senchyna et al. 2019b), we will test whether XRBs are an important contributor to the He II emission observed in low-metallicity galaxies across redshifts.

### 5.2.2. Stripped stars

It has been shown that interacting binary stars, which can result in one of the stars being stripped of its envelope, can emit a significant amount of ionising radiation – He<sup>+</sup> ionisation in particular – and can account for the missing ionising photons in stellar population synthesis models (Götberg et al. 2018, 2019). The effect of stripped stars lasts for a much longer time after the initial starburst, and can provide He<sup>+</sup> ionising photons even at older stellar ages. However, the contribution towards He<sup>+</sup> ionising photons may not be enough even after the inclusion of stripped stars, as the ratio of the emission rate of ionising photons for He II and H I,  $Q_2/Q_0 \sim 10^{-3.7}$ , is still relatively low, for example, showed that  $Q_2/Q_0 \sim 10^{-2}$  is needed to account for the He II / H $\beta$  observations.

### 5.2.3. Wolf-Rayet stars

Broad He II emission has often been attributed to WR stars, both from theoretical (see Schaefer 1996, for example) and observational (Brinchmann et al. 2008) points of view. WR stars are rare, massive stars that have lost their outer hydrogen layer and are in the process of fusing helium or other heavier elements in their core. A characteristic feature of WR stars is the presence of broad emission lines due to fast stellar winds. Schaefer (1996) showed that WR stars can power the broad He II  $\lambda 4686$  emission line observed in galaxies. Shirazi & Brinchmann (2012) showed that WR stars in galaxies with low metallicities and with low stellar ages of 4 – 5 Myr can explain the broad He II emission, but a significant fraction of galaxies with nebular He II emission do not show signatures of the presence of WR stars.

In our sample of He II emitters, there are six galaxies that show broad He II  $\lambda 1640$  (FWHM > 1000 km s<sup>-1</sup>), which could likely be powered by WR stars. However, to confirm that WR stars are indeed powering these sources, looking for the presence of other spectral features associated with WR stars is necessary, such as WR bumps around He II and C IV. In the spectra of sources with broad He II in our sample, we examined the regions around the He II and C IV UV lines but we do not see a bump in the spectrum around these regions. The presence of these bumps is not clear in the stacked spectra either. This is not surprising given the relatively low S/N of the spectra and the low number of galaxies that go into the stack. A full analysis searching for other WR features in the spectra of *Broad* He II emitters is beyond the scope of this work, and deeper observations of the rest-frame optical spectrum of these sources may hold some clues.

### 5.2.4. AGNs

Hard UV ionising photons produced by AGN accretion can provide the energies required to ionise He II. Emission lines originating from AGNs are often very strong and depending on the viewing angle, could also be very broad (FWHM > 1000 km s<sup>-1</sup>). Therefore, sources that show strong and/or broad He II emission in our sample could be powered by AGNs. The UV line ratios of stacked spectra suggest that stacks of the *Broad* He II emitters indeed lie closer to the AGN regime than the star-forming regime (see Figure 6).

Apart from the above, we do not see any clear or obvious signatures of AGNs (for example, the N V line) in the spectra of our galaxies. Strong C IV emission in He II emitters has often been attributed to AGNs (see Nanayakkara et al. 2019, for example), however, as we showed in Section 4.3, BPASS models (Xiao et al. 2018) can explain the line ratios of galaxies with both He II and C IV through star-formation alone, and indeed C IV has been observed in extremely low-metallicity galaxies with He II emission in the local Universe.

Therefore, it is likely that sources with broad He II emission could be powered by AGNs, but with currently available data it is not easy to be certain about the nature of the underlying ionising source. In a follow-up paper we will explore in greater detail the X-ray properties of our He II emitters, and use the X-ray luminosities to confirm or rule-out the presence of AGNs in our sample.

## 6. Conclusions

In this paper we present He II  $\lambda 1640$  -emitting galaxies in the redshift range  $z = 2.2$ – $4.8$  selected from the VANDELS spectroscopic survey in the Chandra Deep Field South (CDFS) and the UKIDSS Ultra Deep Survey (UDS) fields. The sources were selected using a combination of visual examination of both 1D and 2D spectra, as well as emission-line-fitting techniques. Starting from a Parent sample of 949 spectra in the redshift range mentioned above in both fields with secure spectroscopic redshifts, we identified a sample of 33 *Bright* (S/N > 2.5) He II emitters and 17 *Faint* (S/N < 2.5) He II emitters.

For the *Bright* He II emitters, we performed careful measurements of the He II emission line flux, FWHM, and EW. Where detected, we also measured other UV lines in the spectra of these galaxies. For the *Faint* He II emitters, we relied on stacking to infer their properties. We then analysed the physical properties of He II emitting sources, both for individual galaxy spectra and stacks, and used UV emission line ratio diagnostics to set constraints on the underlying ionising mechanisms.

The main conclusions of this study are as follows:

- The measured line fluxes of *Bright* He II emitters in VANDELS range from  $1.1$  to  $31.0 \times 10^{-18}$  erg s<sup>-1</sup> cm<sup>-2</sup>. The FWHM (rest-frame) range from 240 to 2120 km s<sup>-1</sup> and EWs (rest-frame) range from 0.9 to 21.4 Å. The stellar masses inferred from SED fitting using broad-band photometry are in the range  $\log_{10} M_{\star} = 8.6$ – $10.8 M_{\odot}$ , UV corrected star-formation rates are in the range  $\log_{10}(\text{SFR}) = 0.5$  –  $2.0 M_{\odot} \text{ yr}^{-1}$ , and rest-frame UV magnitudes (at 1500 Å are in the range  $M_{\text{UV}} = -21.9$  to  $-19.2$ . When comparing the physical properties with the parent sample using KS tests, we do not see significant differences between galaxies that show strong He II emission and the galaxies with no He II emission in the parent sample.
- We identify seven possible AGNs in our sample of He II emitters, which have been identified either due to the presence



of strong C IV emission in their spectra, or an X-ray match in the publicly available catalogues. Additionally, we separated the *Bright* He II emitters that are not possible AGNs into subsamples based on the FWHM of their He II line, and classify 20 sources as *Narrow* ( $\text{FWHM} < 1000 \text{ km s}^{-1}$ ) and 6 sources as *Broad* ( $\text{FWHM} > 1000 \text{ km s}^{-1}$ ). We then produced stacked spectra of narrow and broad emitters, in addition to a stacked spectrum of faint He II emitters. We then used He II, O III] and C III] lines, both from individual spectra and stacks to compare the observations with stellar population synthesis models. The models we use are from Gutkin et al. (2016) based on single stars, and from Xiao et al. (2018) that take into account the effect of binary stars.

- The predictions from single star models suggest that the line ratios of a majority of our He II emitters, including the stacks of *Narrow* and *Faint* emitters, can be explained by star-formation alone; however, there are degeneracies between the model parameters. Single star models are unable to reproduce the line ratios seen in *Broad* He II emitters, and we show that ionisation from AGNs is preferred for these. However, models including the effect of binaries from Xiao et al. (2018) reproduce the line ratios of all He II emitters in a more consistent manner when compared to single star models. The metallicities of the models that best match the observations are in the range  $Z = 0.0001 - 0.002$  with stellar ages of  $10^7 - 10^8 \text{ yr}$ . Our measured line ratios overlap almost completely with observations in the literature of He II emitters at comparable redshifts, and compared to UV line ratios of local metal-poor dwarf galaxies, the metallicities required to explain our sources are generally lower.
- Although the low-metallicity binary star models are able to reproduce the UV line ratios of our He II emitters, they underpredict the He II EWs. C III] EWs can be reproduced by low-metallicity models with ages below  $10^7$  years, but the EWs of He II are underpredicted by even the lowest metallicity models with young ages, as has been previously reported. This suggests that the inclusion of additional mechanisms capable of producing He II ionising photons is required in stellar population synthesis modelling. Models with solar metallicity underpredict EWs of all UV lines considered in this study by a few orders of magnitude, leading to the conclusion that He II emitters presented in this study are likely to have sub-solar metallicities.
- We measure stellar metallicities on stacks of all He II emitters (*Bright* and *Faint* combined) using features in the UV spectrum, and find a metallicity of  $Z = 0.0022 \pm 0.0003 Z_{\odot}$ , a value that is roughly 10% of the solar metallicity. Interestingly, the metallicity measured for the stack of galaxies that do not show He II emission is  $Z = 0.0020 \pm 0.0002 Z_{\odot}$ , and consistent within error bars with that of He II emitters. This suggests that galaxies that show He II emission are not particularly metal poor when compared to the general galaxy population at these redshifts, but must have undergone a recent star-formation event that also boosts the strength of the other UV lines seen in their spectra.
- We show that additional mechanisms such as a contribution from XRBs or stripped stars may be needed to properly reproduce the observed He II EWs in the spectra of galaxies in our sample. In a follow-up paper, we aim to explore the X-ray properties of He II emitters and set constraints on the XRB contribution in these galaxies.

could be used for comparison in this paper. RS acknowledges support from the Amaldi Research Center funded by the MIUR program "Dipartimento di Eccellenza" (CUP:B81118001170001). This work has made extensive use of PYTHON (Pérez & Granger 2007), ASTROPY (Astropy Collaboration et al. 2013), MATPLOTLIB (Hunter 2007), MPDAF (Bacon et al. 2016) and TOPCAT (Taylor 2005). This work would not have been possible without the countless hours put in by members of the open-source developing community all around the world.

## References

- Amorín, R., Fontana, A., Pérez-Montero, E., et al. 2017, *Nature Astronomy*, 1, 0052
- Astropy Collaboration, Robitaille, T. P., Tollerud, E. J., et al. 2013, *A&A*, 558, A33
- Bacon, R., Piqueras, L., Conseil, S., Richard, J., & Shepherd, M. 2016, MPDAF: MUSE Python Data Analysis Framework, Astrophysics Source Code Library
- Barkana, R. & Loeb, A. 2001, *Phys. Rep.*, 349, 125
- Berg, D. A., Chisholm, J., Erb, D. K., et al. 2019, *ApJ*, 878, L3
- Berg, D. A., Erb, D. K., Auger, M. W., Pettini, M., & Brammer, G. B. 2018, *ApJ*, 859, 164
- Berg, D. A., Skillman, E. D., Henry, R. B. C., Erb, D. K., & Carigi, L. 2016, *ApJ*, 827, 126
- Bergeron, P., Ruiz, M. T., & Leggett, S. K. 1997, *ApJS*, 108, 339
- Bouwens, R. J., Illingworth, G. D., Oesch, P. A., et al. 2015, *ApJ*, 811, 140
- Brinchmann, J., Kunth, D., & Durret, F. 2008, *A&A*, 485, 657
- Bromm, V. & Larson, R. B. 2004, *ARA&A*, 42, 79
- Bromm, V. & Yoshida, N. 2011, *ARA&A*, 49, 373
- Brorby, M., Kaaret, P., Prestwich, A., & Mirabel, I. F. 2016, *MNRAS*, 457, 4081
- Bruzual, G. & Charlot, S. 2003, *MNRAS*, 344, 1000
- Calzetti, D., Armus, L., Bohlin, R. C., et al. 2000, *ApJ*, 533, 682
- Cassata, P., Le Fèvre, O., Charlot, S., et al. 2013, *A&A*, 556, A68
- Cullen, F., Cirasuolo, M., McLure, R. J., Dunlop, J. S., & Bowler, R. A. A. 2014, *MNRAS*, 440, 2300
- Cullen, F., McLure, R. J., Dunlop, J. S., et al. 2019, *MNRAS*, 487, 2038
- Douna, V. M., Pellizza, L. J., Mirabel, I. F., & Pedrosa, S. E. 2015, *A&A*, 579, A44
- Eldridge, J. J., Stanway, E. R., Xiao, L., et al. 2017, *PASA*, 34, e058
- Erb, D. K., Pettini, M., Shapley, A. E., et al. 2010, *ApJ*, 719, 1168
- Feltre, A., Charlot, S., & Gutkin, J. 2016, *MNRAS*, 456, 3354
- Ferland, G. J., Porter, R. L., van Hoof, P. A. M., et al. 2013, *Rev. Mexicana Astron. Astrofis.*, 49, 137
- Finkelstein, S. L., D'Aloisio, A., Paardekooper, J.-P., et al. 2019, *ApJ*, 879, 36
- Fornasini, F. M., Kriek, M., Sanders, R. L., et al. 2019, arXiv e-prints, arXiv:1909.08635
- Fragos, T., Lehmer, B., Tremmel, M., et al. 2013a, *ApJ*, 764, 41
- Fragos, T., Lehmer, B. D., Naoz, S., Zezas, A., & Basu-Zych, A. 2013b, *ApJ*, 776, L31
- Garilli, B., Paioro, L., Scoddeggio, M., et al. 2012, *PASP*, 124, 1232
- Garnett, D. R., Kennicutt, Robert C., J., Chu, Y.-H., & Skillman, E. D. 1991, *ApJ*, 373, 458
- Götberg, Y., de Mink, S. E., Groh, J. H., et al. 2018, *A&A*, 615, A78
- Götberg, Y., de Mink, S. E., Groh, J. H., Leitherer, C., & Norman, C. 2019, *A&A*, 629, A134
- Grogin, N. A., Kocevski, D. D., Faber, S. M., et al. 2011, *ApJS*, 197, 35
- Guseva, N. G., Izotov, Y. I., & Thuan, T. X. 2000, *ApJ*, 531, 776
- Gutkin, J., Charlot, S., & Bruzual, G. 2016, *MNRAS*, 462, 1757
- Henry, A., Scarlata, C., Domínguez, A., et al. 2013, *ApJ*, 776, L27
- Hunter, J. D. 2007, *Computing In Science & Engineering*, 9, 90
- Inoue, A. K. 2003, *PASJ*, 55, 901
- Izotov, Y. I. & Thuan, T. X. 2004, *ApJ*, 602, 200
- Kehrig, C., Vílchez, J. M., Guerrero, M. A., et al. 2018, *MNRAS*, 480, 1081
- Kehrig, C., Vílchez, J. M., Pérez-Montero, E., et al. 2015, *ApJ*, 801, L28
- Kewley, L. J., Nicholls, D. C., & Sutherland, R. S. 2019, *ARA&A*, 57, 511
- Kocevski, D. D., Hasinger, G., Brightman, M., et al. 2018, *ApJS*, 236, 48
- Koekemoer, A. M., Faber, S. M., Ferguson, H. C., et al. 2011, *ApJS*, 197, 36
- Li, Q., Narayanan, D., & Davé, R. 2019, *MNRAS*, 490, 1425
- Luo, B., Brandt, W. N., Xue, Y. Q., et al. 2017, *ApJS*, 228, 2
- Marchi, F., Pentericci, L., Guaita, L., et al. 2018, *A&A*, 614, A11
- McLure, R. J., Pentericci, L., Cimatti, A., et al. 2018, *MNRAS*, 479, 25
- Nakajima, K., Schaerer, D., Le Fèvre, O., et al. 2018, *A&A*, 612, A94
- Nanayakkara, T., Brinchmann, J., Boogaard, L., et al. 2019, *A&A*, 624, A89
- Oke, J. B. & Gunn, J. E. 1983, *ApJ*, 266, 713
- Patrício, V., Richard, J., Verhamme, A., et al. 2016, *MNRAS*, 456, 4191
- Pentericci, L., McLure, R. J., Garilli, B., et al. 2018, *A&A*, 616, A174
- Pérez, F. & Granger, B. E. 2007, *Computing In Science and Engineering*, 9, 21
- Planck Collaboration, Ade, P. A. R., Aghanim, N., et al. 2016, *A&A*, 594, A13
- Robertson, B. E., Ellis, R. S., Dunlop, J. S., McLure, R. J., & Stark, D. P. 2010, *Nature*, 468, 49

*Acknowledgements.* The authors thank the referee for useful and constructive comments that helped improve the quality of this manuscript. AS thanks Themiyana Nanayakkara for useful discussions and for sharing the latest data that



- Robertson, B. E., Ellis, R. S., Furlanetto, S. R., & Dunlop, J. S. 2015, *ApJ*, 802, L19
- Sanders, R. L., Shapley, A. E., Kriek, M., et al. 2018, *ApJ*, 858, 99
- Schaerer, D. 1996, *ApJ*, 467, L17
- Schaerer, D. 2002, *A&A*, 382, 28
- Schaerer, D. 2003, *A&A*, 397, 527
- Schaerer, D., Fragos, T., & Izotov, Y. I. 2019, *A&A*, 622, L10
- Senchyna, P., Stark, D. P., Chevallard, J., et al. 2019a, *MNRAS*, 488, 3492
- Senchyna, P., Stark, D. P., Mirocha, J., et al. 2019b, *arXiv e-prints*, arXiv:1909.10574
- Senchyna, P., Stark, D. P., Vidal-García, A., et al. 2017, *MNRAS*, 472, 2608
- Shapley, A. E., Steidel, C. C., Pettini, M., & Adelberger, K. L. 2003, *ApJ*, 588, 65
- Shirazi, M. & Brinchmann, J. 2012, *MNRAS*, 421, 1043
- Sobral, D., Matthee, J., Darvish, B., et al. 2015, *ApJ*, 808, 139
- Sokasian, A., Yoshida, N., Abel, T., Hernquist, L., & Springel, V. 2004, *MNRAS*, 350, 47
- Stanway, E. R. & Eldridge, J. J. 2018, *MNRAS*, 479, 75
- Stanway, E. R. & Eldridge, J. J. 2019, *A&A*, 621, A105
- Stanway, E. R., Eldridge, J. J., & Becker, G. D. 2016, *MNRAS*, 456, 485
- Steidel, C. C., Rudie, G. C., Strom, A. L., et al. 2014, *ApJ*, 795, 165
- Steidel, C. C., Strom, A. L., Pettini, M., et al. 2016, *ApJ*, 826, 159
- Székési, D., Langer, N., Yoon, S.-C., et al. 2015, *A&A*, 581, A15
- Taylor, M. B. 2005, in *Astronomical Society of the Pacific Conference Series*, Vol. 347, *Astronomical Data Analysis Software and Systems XIV*, ed. P. Shopbell, M. Britton, & R. Ebert, 29
- Topping, M. W., Shapley, A. E., Reddy, N. A., et al. 2019, *arXiv e-prints*, arXiv:1912.10243
- Tumlinson, J. & Shull, J. M. 2000, *ApJ*, 528, L65
- Wise, J. H., Turk, M. J., Norman, M. L., & Abel, T. 2012, *ApJ*, 745, 50
- Xiao, L., Stanway, E. R., & Eldridge, J. J. 2018, *MNRAS*, 477, 904

## Appendix A: Rest-frame spectra of *Bright* He II emitters

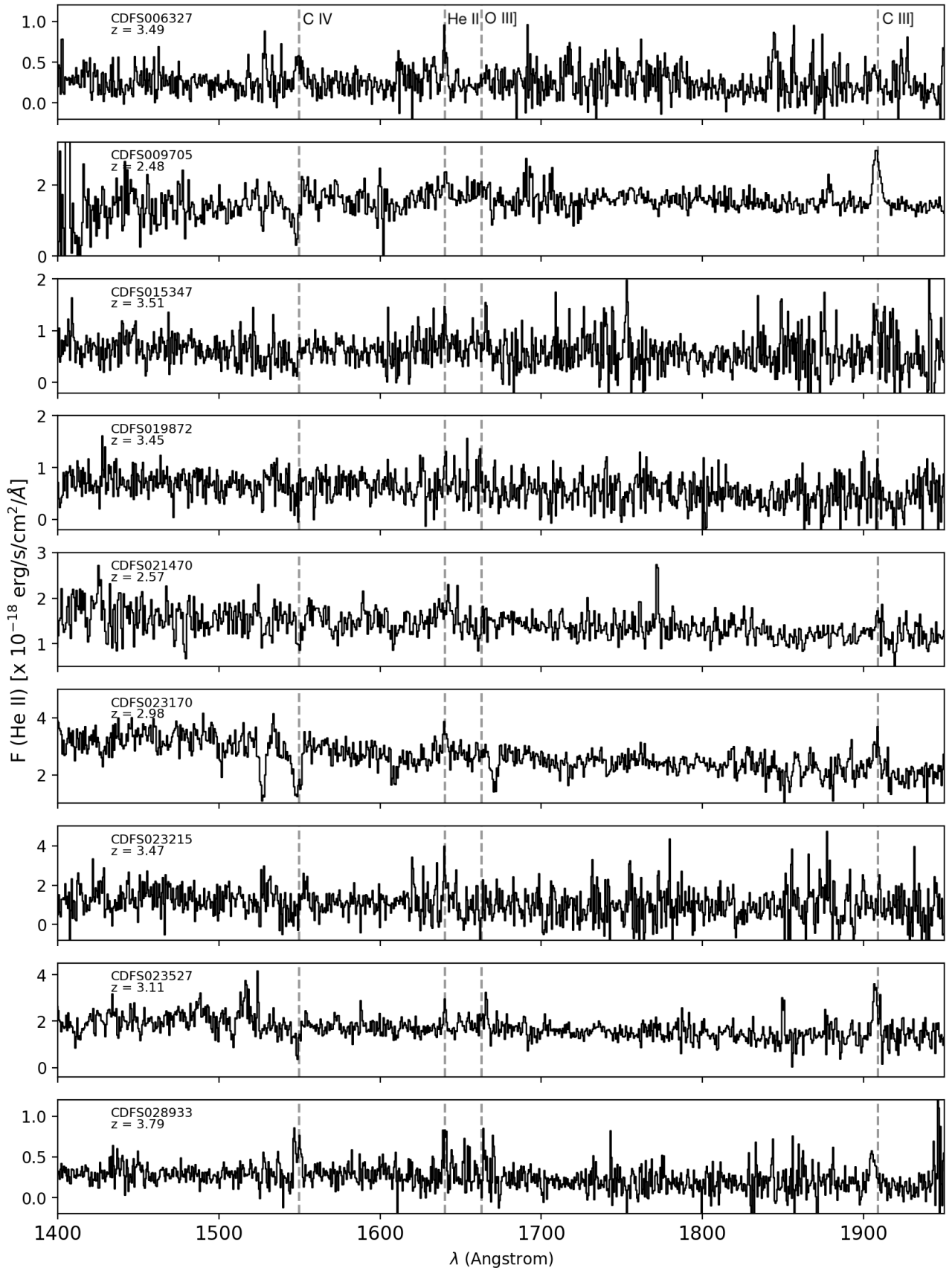


Fig. A.1: Rest frame spectra of *Bright* ( $S/N > 2.5$ ) He II emitters identified in the CDFS and UDS fields. Also marked in the spectra are other rest-frame UV emission lines used in this study.

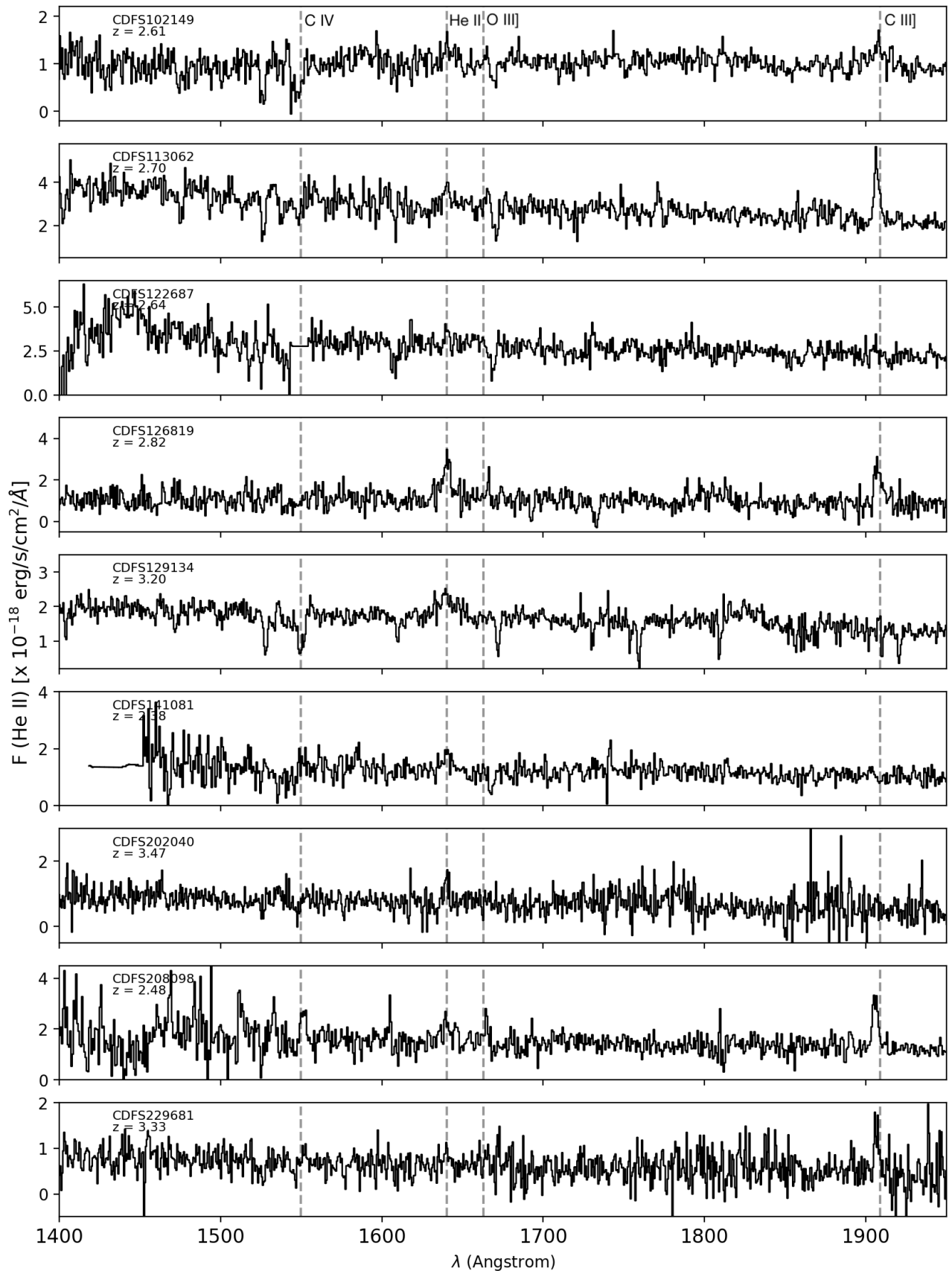


Fig. A.1: (continued)

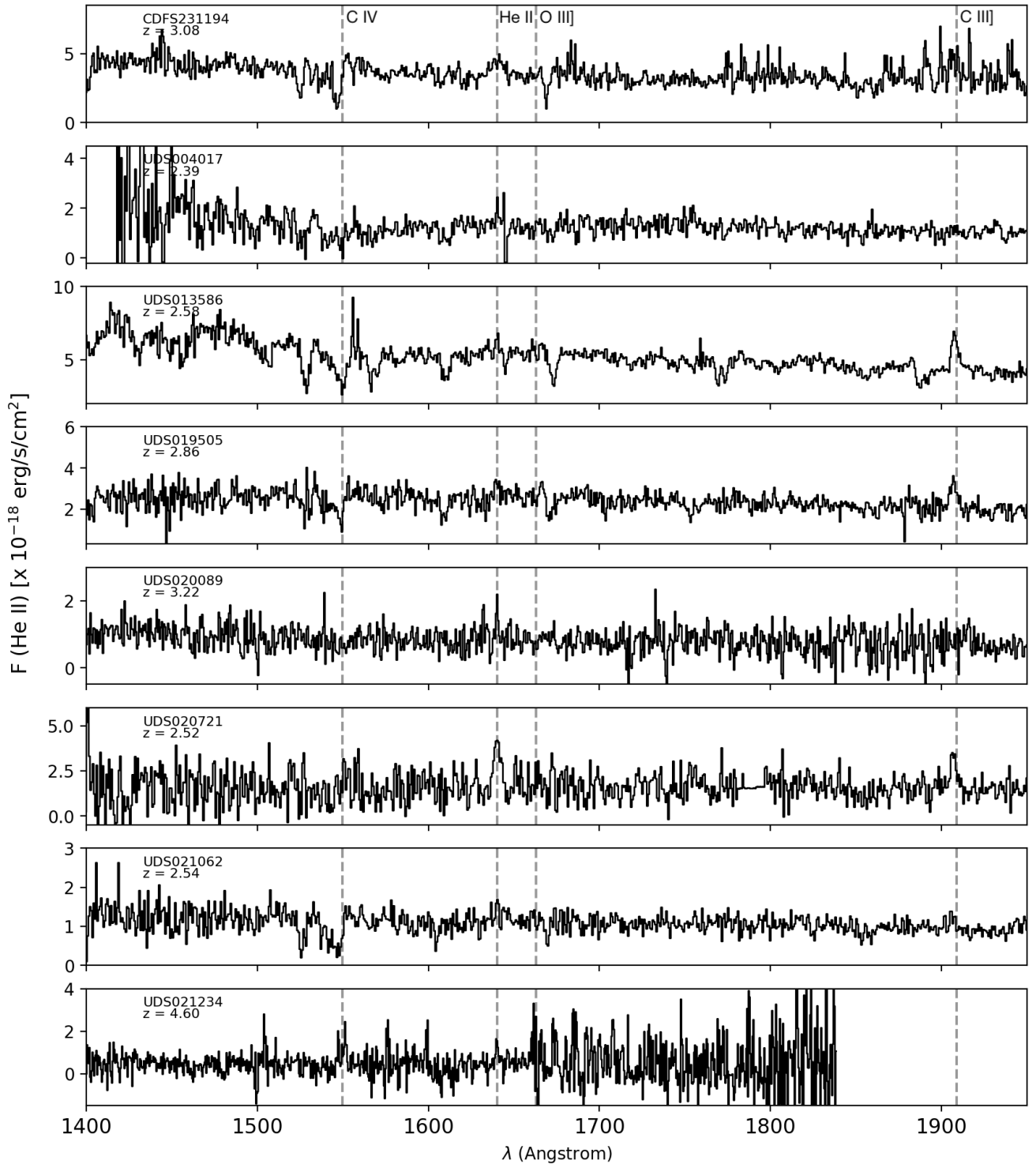


Fig. A.1: (continued)



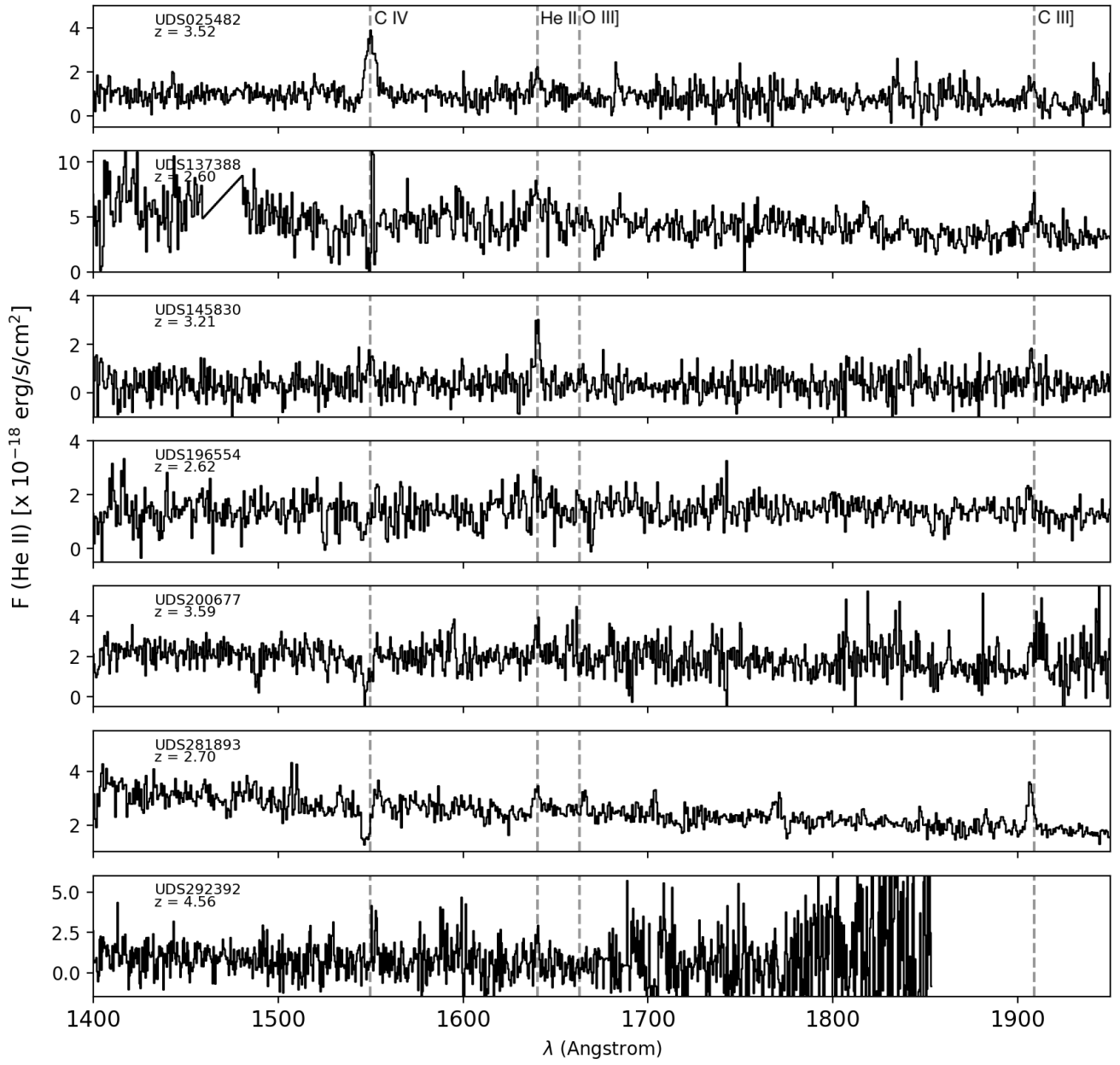


Fig. A.1: (continued)